

# Numerical Heat Transfer, Part A: Applications

## An International Journal of Computation and Methodology

ISSN: 1040-7782 (Print) 1521-0634 (Online) Journal homepage: <https://www.tandfonline.com/loi/unht20>

## Real-time temperature estimation with enhanced spatial resolution during MR-guided hyperthermia therapy

César C. Pacheco, Helcio R. B. Orlande, Marcelo J. Colaço, George S. Dulikravich, Leonardo A. B. Varón & Bernard Lamien

To cite this article: César C. Pacheco, Helcio R. B. Orlande, Marcelo J. Colaço, George S. Dulikravich, Leonardo A. B. Varón & Bernard Lamien (2020): Real-time temperature estimation with enhanced spatial resolution during MR-guided hyperthermia therapy, Numerical Heat Transfer, Part A: Applications, DOI: [10.1080/10407782.2020.1720409](https://doi.org/10.1080/10407782.2020.1720409)

To link to this article: <https://doi.org/10.1080/10407782.2020.1720409>



Published online: 04 Feb 2020.



Submit your article to this journal [↗](#)



View related articles [↗](#)



View Crossmark data [↗](#)



# Real-time temperature estimation with enhanced spatial resolution during MR-guided hyperthermia therapy

César C. Pacheco<sup>a,b</sup> , Helcio R. B. Orlando<sup>b</sup> , Marcelo J. Colaço<sup>b</sup> , George S. Dulikravich<sup>c</sup> , Leonardo A. B. Varón<sup>b,d</sup> , and Bernard Lamien<sup>b,e</sup> 

<sup>a</sup>Department of Mechanical Engineering, Federal Fluminense University – PGMEC/UFF, Niterói, Brazil;

<sup>b</sup>Department of Mechanical Engineering, Federal University of Rio de Janeiro – COPPE/UFRJ, Brazil;

<sup>c</sup>Department of Mechanical and Materials Engineering, Florida International University – MAIDROC Laboratory, FIU, Miami, USA; <sup>d</sup>Department of Bioengineering, Universidad Santiago de Cali, Colombia; <sup>e</sup>École Polytechnique de Ouagadougou (EPO), Ouagadougou, Burkina Faso

## ABSTRACT

In this article, the temperature of biological tissues is estimated during hyperthermia therapy, while accounting for uncertainties in the bioheat transfer problem and in the available measurements. A state estimation problem is solved with the Steady-State Kalman Filter. The Pennes bioheat transfer model and the PRF-Shift Magnetic Resonance Thermometry are used as evolution and observation models, respectively. Instead of using the direct inversion of the measured data as with the PRF-Shift Magnetic Resonance Thermometry, the state-estimation framework allows for enhancing the spatial resolution of the estimated temperature variation and reducing the related uncertainties. Since the time consuming steps of the Steady-State Kalman Filter can be performed offline, the recursive solution of the state estimation problem is performed with computational times smaller than the simulated physical times. Synthetic measurements are used for the state estimation problem in a region of the human forearm, for radiofrequency and laser-diode heat sources of the hyperthermia therapy.

## ARTICLE HISTORY

Received 2 September 2019

Accepted 17 January 2020

## 1. Introduction

One of the main objectives in oncology research has been the development of minimally invasive or noninvasive cancer treatment protocols in order to reduce risk of post-surgical complications, patient's recovery time and cost [1]. Although noninvasive treatments are already clinically available, new methods have been recently under development, including hyperthermia, where heat is applied to make the tumor more vulnerable to cytotoxic agents or to directly kill the cancerous cells by necrosis [2–3]. Hyperthermia aims at increasing the temperature of tumor cells, while allowing only minimal thermal damage to healthy cells [4–7]. Therefore, real-time monitoring of the temperature in the region containing the tumor is required for a successful and safe hyperthermia treatment. Magnetic resonance thermometry (MRT) [2, 8] has been used for the measurement of the internal temperature of the body, by means of the PRF-Shift method developed by Ishihara *et al.* [9]. Such method can be used with conventional magnetic resonance (MR) equipment currently found in most hospitals. However, the MR measured data is commonly inverted with an algebraic equation to recover the local internal body temperature in the

## Nomenclature

<b>A</b>	surface area of the tumor ( $\text{m}^2$ )	<b>x</b>	state vector ( $^{\circ}\text{C}$ )
<b>B<sub>0</sub></b>	external magnetic field (T)	<b>y</b>	observation vector (degree)
<b>c<sub>b</sub></b>	specific heat of blood per unit of mass ( $\text{J kg}^{-1} ^{\circ}\text{C}^{-1}$ )	<b>Greek letters</b>	
<b>c<sub>p</sub></b>	specific heat of tissues per unit mass ( $\text{J kg}^{-1} ^{\circ}\text{C}^{-1}$ )	$\alpha$	temperature dependence of chemical shift ( $\text{ppm } ^{\circ}\text{C}^{-1}$ )
<b>E</b>	electric field ( $\text{V m}^{-1}$ )	$\beta_{tr}$	transport attenuation coefficient ( $\text{m}^{-1}$ )
<b>E<sub>0</sub></b>	maximum laser irradiance at the boundary ( $\text{W m}^{-2}$ )	$\gamma$	gyromagnetic ratio ( $\text{MHz T}^{-1}$ )
<b>F</b>	evolution matrix	$\Delta T$	temperature increase ( $^{\circ}\text{C}$ )
<b>f</b>	frequency of electric field waves (Hz)	$\Delta t$	time step (s)
<b>f<sub>a</sub></b>	anisotropy factor	$\Delta\Phi$	phase shift (degree)
<b>g<sub>h</sub></b>	external volumetric heat generation ( $\text{W m}^{-3}$ )	$\partial\Omega$	boundary of physical domain
<b>g<sub>m</sub></b>	metabolic volumetric heat generation ( $\text{W m}^{-3}$ )	$\epsilon_r$	relative electric permittivity ( $\text{F m}^{-1}$ )
<b>H</b>	observation matrix	$\theta$	concentration of nanoparticles
<b>h</b>	heat transfer coefficient ( $\text{W m}^{-2} ^{\circ}\text{C}^{-1}$ )	$\kappa$	laser energy absorption coefficient ( $\text{m}^{-1}$ )
<b>K</b>	Kalman gain matrix	$\mu_0$	magnetic permeability of vacuum ( $\text{H m}^{-1}$ )
<b>k</b>	thermal conductivity ( $\text{W m}^{-1} ^{\circ}\text{C}^{-1}$ )	$\xi_s$	scattering coefficient ( $\text{m}^{-1}$ )
<b>k<sub>e</sub></b>	electrical conductivity ( $\text{S m}^{-1}$ )	$\xi_s'$	reduced scattering coefficient ( $\text{m}^{-1}$ )
<b>M</b>	magnetization ( $\text{A m}^{-2}$ )	$\pi$	probability density function
<b>P</b>	covariance matrix of the estimated state variables	$\rho$	density of tissues ( $\text{kg m}^{-3}$ )
<b>Q</b>	covariance matrix of the evolution model	$\rho_b$	density of blood ( $\text{kg m}^{-3}$ )
<b>R</b>	covariance matrix of the observation model	$\chi$	magnetic susceptibility of nanoparticles ( $\text{kg m A}^{-2}$ )
<b>R</b>	magnetic induction loop radius (m)	$\varphi$	total fluence rate ( $\text{W m}^{-2}$ )
<b>r</b>	position vector (m)	$\varphi_p$	primary fluence rate ( $\text{W m}^{-2}$ )
<b>s</b>	chemical shift	$\varphi_s$	secondary fluence rate ( $\text{W m}^{-2}$ )
<b>T</b>	temperature ( $^{\circ}\text{C}$ )	$\Omega$	physical domain
<b>T<sub>a</sub></b>	arterial blood temperature ( $^{\circ}\text{C}$ )	$\omega$	angular speed ( $\text{rad s}^{-1}$ )
<b>T<sub>0</sub></b>	baseline temperature ( $^{\circ}\text{C}$ )	$\omega_b$	blood perfusion rate in the tissue ( $\text{s}^{-1}$ )
<b>T<sub>∞</sub></b>	external temperature ( $^{\circ}\text{C}$ )	<b>Superscripts</b>	
<b>t</b>	time (s)	+	posterior
<b>t<sub>E</sub></b>	echo time (s)	−	prior
<b>u</b>	electric potential (V)	^	estimate
<b>v</b>	observation noise vector (degree)	<b>Subscripts</b>	
<b>w</b>	state noise vector ( $^{\circ}\text{C}$ )	$\infty$	value at steady-state
		$n$	time $t_n$

PRF-Shift method. Therefore, measurement uncertainties are directly propagated to the estimated temperatures, which are usually quite noisy. In this article, the temperature is recovered through the solution of a state estimation problem [7, 10–13]. It deals with uncertainties in the evolution and observation models, thus, reducing inaccuracies and instabilities inherent to the direct inversion of the magnetic resonance data. The state estimation problem is solved with an asymptotic version of the Kalman filter, referred to as Steady-State Kalman Filter (SSKF) [14–16]. This version results in a significant reduction of the computational effort of the Kalman filter. Recently, we demonstrated that SSKF can be applied in real-time monitoring of the internal body temperature with uncertainties much smaller than those resulting from the direct inversion of the MR data [14]. In this article, we extend our previous work [14] to include two possible hyperthermia treatments, based on radio frequency [17–22] or laser heat sources [23–26]. The cases considered here involve simulated measurements in the region of interest around the tumor, on a mesh much coarser than that used for the estimation of the state vector. Therefore, the spatial

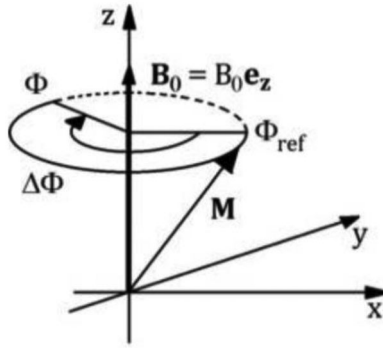


**Figure 1.** Precession of the global magnetization  $\mathbf{M}$  around the axis of the external magnetic field  $\mathbf{B}_0$  (modified from Kuperman [33]).

resolution of the recovered transient temperature field can be enhanced with the solution of the state estimation problem, as demonstrated below.

## 2. Magnetic resonance thermometry

The application of magnetic resonance (MR) techniques to nonintrusive thermometry has been of interest of the radiology community for almost 70 years, since the temperature dependence of the chemical shift was first documented [2, 27]. The Proton Resonance Shift (PRF-shift) thermometry [9] became the most widely used and accepted method for performing measurements of the internal body temperature using magnetic resonance. Although other techniques have also been developed, for example, based on the longitudinal relaxation time  $t_1$  [28] and on the molecular diffusion coefficient [29], they are outperformed by the PRF-Shift method [2, 30].

The basic principle of magnetic resonance is associated with the fact that atomic nuclei with nonzero spin present a natural frequency when subjected to an external magnetic field,  $\mathbf{B}_0$ . Such nuclei have an intrinsic magnetic moment that, in the presence of  $\mathbf{B}_0$ , performs a precession movement around the axis of  $\mathbf{B}_0$ . Under such conditions, excitation of an atomic nucleus by an AC magnetic field  $\mathbf{B}_1$  with frequency  $\omega$  results in the magnetic resonance phenomenon. This process is illustrated by Figure 1, where the magnetization,  $\mathbf{M}$ , represents the magnetic moment density [31]. The precession movement has a well-defined frequency, called Larmor frequency [32], given by

$$\omega = \gamma B_0 \quad (1)$$

where  $\gamma$  is the gyromagnetic ratio.

Atomic nuclei are surrounded by electrons, which induce a secondary magnetic field. Therefore, the global magnetic field experienced by the nuclei is expected to deviate slightly from  $\mathbf{B}_0$  and the respective Larmor frequency is different from that given by Eq. (1). The local magnetic field and the Larmor frequency are, thus, given respectively by:

$$B(\mathbf{r}) = [1 - s(\mathbf{r})]B_0 \quad (2a)$$

$$\omega(\mathbf{r}) = [1 - s(\mathbf{r})]\gamma B_0 \quad (2b)$$

where  $s(\mathbf{r})$  is called the chemical shift.

The PRF-Shift method is a MRT technique based on the temperature dependence of the chemical shift. In the temperature range from  $-15^\circ\text{C}$  to  $100^\circ\text{C}$ , the chemical shift can be considered as a linear function of temperature and independent of the tissue (except for fat) [9, 33]. Note

that this range includes the temperatures of interest for hyperthermia treatments. Therefore, we can write

$$\frac{\partial s(\mathbf{r}, T)}{\partial T(\mathbf{r})} = \alpha \quad (3)$$

where typically  $\alpha = -0.01 \text{ ppm } ^\circ\text{C}^{-1}$  [2, 8].

Eqs. (2b) and (3) show that changes of the tissue temperature promote variations of the Larmor frequency. Hence, during the precession movement  $\mathbf{M}$  performs a different angular displacement  $\Delta\Phi$ , which is called the phase-shift. Consider a tissue at a temperature  $T_0$  and later at a temperature  $T$ . The temperature variation is related to the variation of the phase-shift by [2, 8, 9]

$$\Delta T(\mathbf{r}, t) = T(\mathbf{r}, t) - T_0(\mathbf{r}) = \frac{\Delta\Phi(T, \mathbf{r}, t) - \Delta\Phi(T_0, \mathbf{r})}{\alpha\gamma B_0 t_E} \quad (4)$$

where  $\Delta\Phi(T)$  can be measured in standard MR equipment using gradient-echo (GRE) pulse sequences, where  $t_E$  is the echo time.

Eq. (4) shows that the PRF-Shift method can be used to measure the temperature variation,  $\Delta T(\mathbf{r}, t)$ . In practice,  $\Delta\Phi(T_0, \mathbf{r})$  is initially measured for the local temperature  $T_0(\mathbf{r})$  before the hyperthermia treatment. Then,  $\Delta\Phi(T, \mathbf{r}, t)$  is measured during the treatment to recover  $\Delta T(\mathbf{r}, t)$  with Eq. (4).

On the other hand, we follow here the technique advanced in our previous work [14] and solve a state estimation problem, in order to avoid the direct inversion of the measured  $\Delta\Phi(T, \mathbf{r}, t)$  to recover the local body temperature variation. The mathematical formulations of the phenomena involved in the hyperthermia treatment and in the measurement of some dependent variable of the system are required for the solution of state estimation problems. Eq. (4) is used as the observation model, while the bioheat transfer model used in this work is described next.

### 3. Bioheat transfer model

The classical Pennes bioheat transfer model [34] is used here for the hyperthermia treatment on an actual geometry of the right forearm, obtained from the Visual Human Dataset (VHD) [35, 36] (see Figure 2). For the present problem, blood flow through major vessels was neglected. Different tissues in the region were taken into account by the physical properties that were considered as position dependent. The region is initially at the temperature  $T_0(\mathbf{r})$ . The boundary surface is supposed to exchange heat by convection and linearized radiation with the surroundings at temperature  $T_\infty$ , with a heat transfer coefficient,  $h$ . The bioheat transfer mathematical model is given by:

$$\begin{aligned} \rho(\mathbf{r})c_p(\mathbf{r})\frac{\partial T(\mathbf{r}, t)}{\partial t} &= \nabla \cdot [k(\mathbf{r})\nabla T(\mathbf{r}, t)] + \\ &+ \omega_b(\mathbf{r})\rho_b c_b [T_a - T(\mathbf{r}, t)] + g_m(\mathbf{r}) + g_h(\mathbf{r}, t), \quad \mathbf{r} \in \Omega, t \geq 0 \end{aligned} \quad (5a)$$

$$k(\mathbf{r})\frac{\partial T(\mathbf{r}, t)}{\partial \mathbf{n}} + hT = hT_\infty, \quad \mathbf{r} \in \partial\Omega, t \geq 0 \quad (5b)$$

$$T(\mathbf{r}, t) = T_0(\mathbf{r}), \quad \mathbf{r} \in \Omega, t = 0 \quad (5c)$$

The three volumetric heat generation terms in Eq. (5a) correspond to blood perfusion, metabolic heat generation, and heating during the hyperthermia treatment, respectively. For convenience in the analysis, since the PRF-Shift method gives the temperature variation,  $\Delta T(\mathbf{r}, t)$  (see Eq. 4), it is possible to write

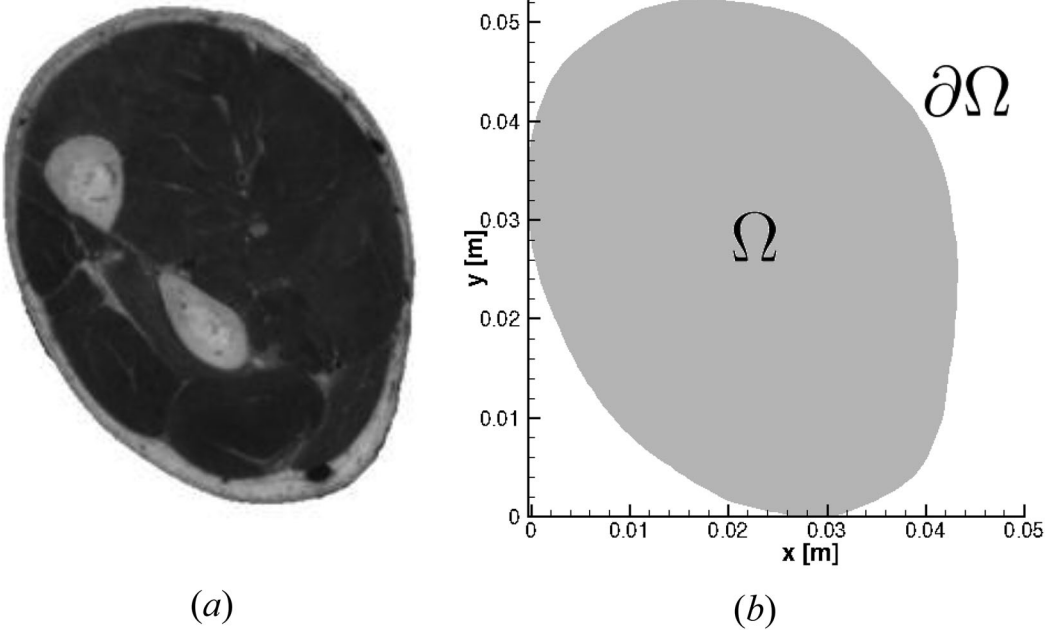


**Figure 2.** Geometry of the problem: (a) transversal section of right human forearm, obtained from VHD [35, 36] and (b) physical model with dimensions.

$$T(\mathbf{r}, t) = T_0(\mathbf{r}) + \Delta T(\mathbf{r}, t) \quad (6)$$

Here,  $T_0(\mathbf{r})$  is obtained from the solution of the following steady-state problem, which corresponds to the bioheat transfer problem before heating is imposed in the hyperthermia treatment:

$$\nabla \cdot [k(\mathbf{r}) \nabla T_0(\mathbf{r})] + \omega_b(\mathbf{r}) \rho_b c_b [T_a - T_0(\mathbf{r})] + g_m(\mathbf{r}) = 0, \quad \mathbf{r} \in \Omega \quad (7a)$$

$$k(\mathbf{r}) \frac{\partial T_0(\mathbf{r})}{\partial \mathbf{n}} + h T_0(\mathbf{r}) = h T_\infty, \quad \mathbf{r} \in \partial \Omega \quad (7b)$$

By using Eqs. (5)–(7), we obtain the following problem for  $\Delta T(\mathbf{r}, t)$ :

$$\rho(\mathbf{r}) c_p(\mathbf{r}) \frac{\partial \Delta T(\mathbf{r}, t)}{\partial t} = \nabla \cdot \{k(\mathbf{r}) \nabla [\Delta T(\mathbf{r}, t)]\} - \omega_b(\mathbf{r}) \rho_b c_b \Delta T(\mathbf{r}, t) + g_h(\mathbf{r}, t), \quad (8a)$$

$$\mathbf{r} \in \Omega, t > 0$$

$$k(\mathbf{r}) \frac{\partial \Delta T(\mathbf{r}, t)}{\partial \mathbf{n}} + h \Delta T(\mathbf{r}, t) = 0, \quad \mathbf{r} \in \partial \Omega, t > 0 \quad (8b)$$

$$\Delta T(\mathbf{r}, t) = 0, \quad \mathbf{r} \in \Omega, t = 0 \quad (8c)$$

For the idealized cases examined in this work, the region shown by Figure 2 was represented in terms of three tissues, namely: dermis/epidermis, muscle and bone/bone marrow, as illustrated by Figure 3a. This figure also shows a circular region in the muscle that mimics a tumor to be heated during the hyperthermia treatment. The bioheat transfer problems given by Eqs. (7) and (8) were discretely solved on an unstructured mesh (see Figure 3b), generated with the GMsh software [37]. The numerical solution of the bioheat transfer problem was obtained by finite volumes [38] with the cross-diffusion correction term from Mathur and Murthy [39]. Code and solution verification can be found in [14].

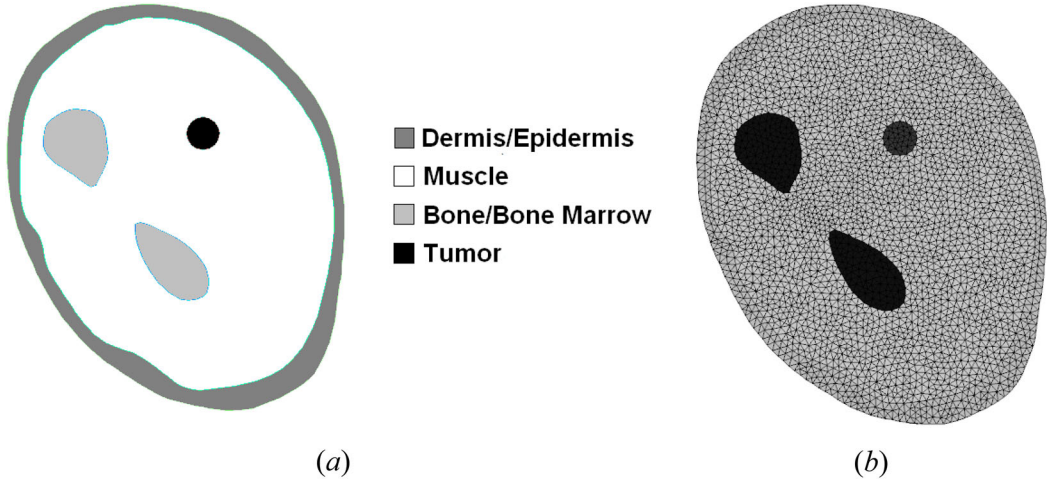


**Figure 3.** Tissue distribution among the physical domain: (a) separation by tissue type and (b) unstructured triangular grid used in the Finite Volume Method.

The two heating models examined in this work for the hyperthermia treatment are described below. They involve heating in the radiofrequency range by using electrodes located on the skin surface of the forearm, as well as heating imposed by a laser-diode in the near-infrared range.

### 3.1. Radiofrequency heating

For the heating in the radiofrequency range, electromagnetic waves are usually imposed in frequencies between 3 kHz and 300 GHz, by using electrodes located on the surface of the body [18, 40]. Magnetic nanoparticles are also used to improve the localized heating in the tumor region and avoid thermal damage to the healthy cells [18, 38], so that the resulting volumetric heat source resulting from the external radiofrequency source is written as [18, 40]

$$g_h(\mathbf{r}) = \left[ (1 - \theta) \frac{k_e}{2} + \theta \frac{9}{16} \frac{\chi''}{\mu_0 \pi f R^2} \right] |\mathbf{E}(\mathbf{r})|^2 \quad (9)$$

The combined Joule heating in the polarizable and magnetizable media given by Eq. (9) is assumed to be time-invariant, where  $k_e$  is the electric conductivity of the local tissue,  $\chi''$  is the magnetic susceptibility of the nanoparticles,  $\mu_0$  is the magnetic permeability of the free space,  $f$  is the externally applied electric field frequency,  $R$  is the radius of the magnetic induction loop and  $\mathbf{E}$  is the local value of the electric field. The concentration of the nanoparticles in the tumor is  $\theta = \pi n r^2 / A$ , where  $A$  is the tumor area.

The electric field can be written as a function of the electric potential,  $u$ , that is,

$$\mathbf{E}(\mathbf{r}) = -\nabla u \quad (10)$$

For the frequencies of the imposed electric field that are commonly used for the hyperthermia treatment, the electric potential can be obtained from the solution of the Gauss's equation for polarizable media:

$$\nabla \cdot [\varepsilon_r(\mathbf{r}) \nabla u(\mathbf{r})] = 0, \quad \mathbf{r} \in \Omega \quad (11a)$$

Two electrodes were considered for the heating in the radiofrequency range, with voltages  $u^+$  and  $u^-$  imposed uniformly over  $\partial\Omega_1$  and  $\partial\Omega_2$ , respectively, as shown in Figure 4. The remaining boundary surface is electrically insulated, so that boundary conditions for Eq. (11a) can be written as

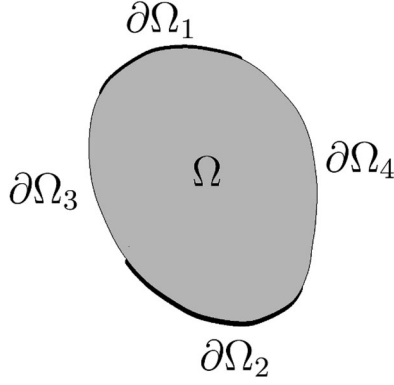


**Figure 4.** Sketch of the electrodes used for the radiofrequency heating model.

$$u = u^+, \quad \mathbf{r} \in \partial\Omega_1 \quad (11b)$$

$$u = u^-, \quad \mathbf{r} \in \partial\Omega_2 \quad (11c)$$

$$\frac{\partial u}{\partial \mathbf{n}} = 0, \quad \mathbf{r} \in \partial\Omega_3 \cup \partial\Omega_4 \quad (11d)$$

### 3.2. Laser heating

The model for the laser heating in the near-infrared range used in this work is based on references [23, 26, 41]. We assume a time invariant heat source, resulting from light propagation and absorption by the tissue, so that,

$$g_h(\mathbf{r}) = \kappa(\mathbf{r})\varphi(\mathbf{r}) \quad (12)$$

where  $\kappa(\mathbf{r})$  is the laser energy absorption coefficient and  $\varphi(\mathbf{r})$  is the laser fluence rate. The fluence rate is split into collimated (primary) and diffusive (secondary) contributions,  $\varphi_p(\mathbf{r})$  and  $\varphi_s(\mathbf{r})$ , respectively, where

$$\varphi(\mathbf{r}) = \varphi_p(\mathbf{r}) + \varphi_s(\mathbf{r}) \quad (13)$$

The primary fluence rate is associated to the collimated fluence whose behavior is described by Beer-Lambert's Law [23], given by Eq. (14a), where  $\beta_{tr}$  is the transport attenuation coefficient and  $\eta$  is the independent spatial variable in the direction of the collimated light propagation applied locally orthogonal inwards on the surface of the forearm. The attenuation coefficient is given by Eq. (14b), where  $\xi'_s$  is the reduced scattering coefficient, calculated with Eq. (14c),  $\xi_s$  is the scattering coefficient, and  $f_a$  is the anisotropy factor.

$$\frac{d\varphi_p(\eta)}{d\eta} = -\beta_{tr}(\eta)\varphi_p, \quad \eta > 0 \quad (14a)$$

$$\beta_{tr} = \kappa + \xi'_s \quad (14b)$$

$$\xi'_s = (1 - f_a^2)\xi_s \quad (14c)$$

The boundary condition specified for the collimated contribution of the fluence rate at the surface of the forearm,  $\eta = 0$ , is given by [23]

$$\varphi_p = E_0, \quad \eta = 0 \quad (14d)$$



The  $\delta$ -P1 diffusion approximation is used for the diffusive fluence rate,  $\varphi_s(\mathbf{r})$  [23]. The mathematical formulation for this boundary value problem is given by [23, 41]

$$\nabla \cdot \left[ -D(\mathbf{r}) \nabla \varphi_s + \frac{\xi_s'(\mathbf{r}) f_a'(\mathbf{r})}{\beta_{tr}(\mathbf{r})} \varphi_p(\mathbf{r}) \mathbf{e}_s \right] + \kappa(\mathbf{r}) \varphi_s(\mathbf{r}) = \xi_s' \varphi_p(\mathbf{r}), \quad \mathbf{r} \in \Omega \quad (15a)$$

$$-D(\mathbf{r}) \frac{\partial \varphi_s(\mathbf{r})}{\partial \mathbf{n}} + \frac{1}{2A_1} \varphi_s(\mathbf{r}) = -\frac{\xi_s'(\mathbf{r}) f_a'(\mathbf{r})}{\beta_{tr}(\mathbf{r})} \varphi_p(\mathbf{r}), \quad \mathbf{r} \in \partial\Omega \quad (15b)$$

where

$$D = \frac{1}{3\beta_{tr}} \quad (15c)$$

$$f_a' = \frac{f_a}{1 + f_a} \quad (15d)$$

$$A_1 = \frac{1 + R_2}{1 - R_1} \quad (15e)$$

In Eqs. (16a)–(16e),  $D$  is the laser light diffusion coefficient,  $\mathbf{e}_s$  is the unit vector at the direction  $\eta$  of propagation of the collimated laser beam,  $A_1$  is the Fresnel coefficient, while  $R_1$  and  $R_2$  are the first and second moment of the Fresnel reflection coefficient, respectively [23, 41].

#### 4. State estimation problem

The mathematical models described so far constitute the *forward (direct) problem*, in which the temperature variation field is evaluated after defining initial and boundary conditions, geometry, thermal properties and heat sources. On the other hand, this work is aimed at using these mathematical models and the phase-shift measurements obtained from magnetic resonance equipment in order to estimate the temperature in the whole domain,  $\Omega$ , during a hyperthermia treatment. Such an *inverse problem* is solved here as a *state estimation problem* within the Bayesian framework of statistics [10–16]. The state vector,  $\mathbf{x}$ , in this work is given by the values of temperature variations in each of the control volumes in the numerical mesh used for the domain discretization, while the observation vector,  $\mathbf{y}$ , contains the phase-shift measurements, that is,

$$\mathbf{x} = \Delta \mathbf{T}(\mathbf{r}, t) \quad (16a)$$

$$\mathbf{y} = \Delta \Phi(\mathbf{T}, \mathbf{r}, t) - \Delta \Phi(\mathbf{T}_0, \mathbf{r}) \quad (16b)$$

In this work, these vectors are assumed to evolve in time by respectively following evolution and observation linear models, with additive Gaussian noises, that is,

$$\mathbf{x}_n = \mathbf{F}_{n-1} \mathbf{x}_{n-1} + \mathbf{s}_n + \mathbf{w}_n \quad (17a)$$

$$\mathbf{y}_n = \mathbf{H}_n \mathbf{x}_n + \mathbf{v}_n \quad (17b)$$

Here, the subscript  $n$  denotes a time instant,  $t_n$ ,  $\mathbf{F}$  is the evolution matrix,  $\mathbf{s}$  is a vector that contains the external excitations (such as boundary conditions and heat sources),  $\mathbf{H}$  is the observation matrix, while  $\mathbf{w}$  and  $\mathbf{v}$  are the noise vectors for the evolution and observation models, respectively. These forms of noise vectors are assumed to follow a Gaussian distribution with zero mean and known covariance matrices  $\mathbf{Q}_n$  and  $\mathbf{R}_n$ , respectively.

The evolution matrix,  $\mathbf{F}$ , results from the numerical discretization of Eqs. (8a)–(8c) via the implicit finite volume method. On the other hand, the observation matrix,  $\mathbf{H}$ , depends on the region where the phase-shift measurements are available for the solution of the state estimation

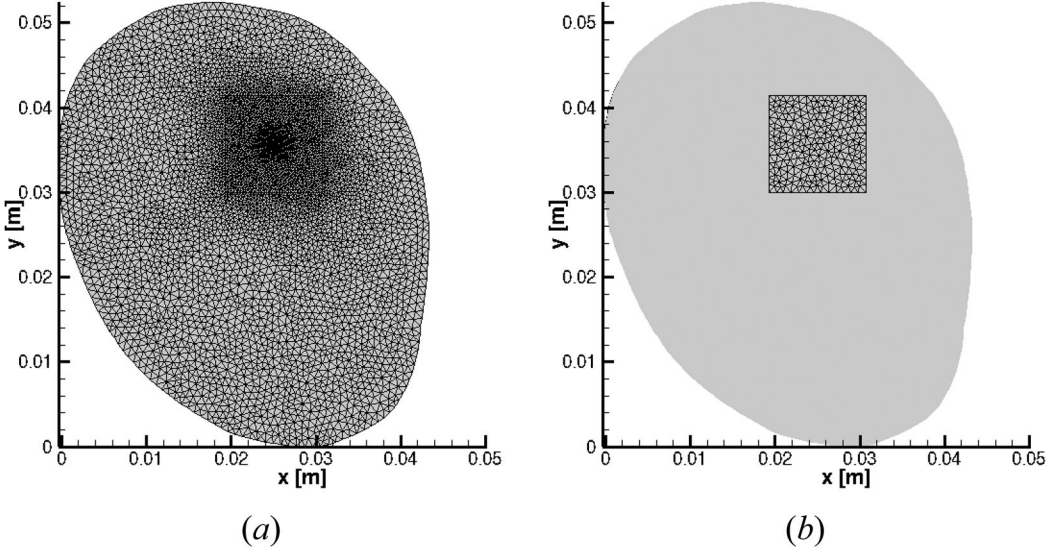


**Figure 5.** Numerical meshes for (a) state vector and (b) observation vector.

problem. Consider, for example, that measurements are available on the same finite volumes used for the evolution model. Thus, we can write (see also Eq. 4):

$$\mathbf{H}_n = -\alpha\gamma t_E B_0 \mathbf{I} \quad (18)$$

where  $\mathbf{I}$  is the identity matrix. On the other hand, the measurements may be focused on a special Region of Interest (ROI) where the most important phenomena take place, thus, avoiding an excessive amount of measured data and unnecessary computational work. For the present application, the ROI is the region around the tumor (see Figure 3), where the largest temperature variations take place due to the hyperthermia treatment. With the state estimation approach used in this work, it is also possible to use measurements from a coarse mesh and then estimate the state vector on a more refined mesh [14].

The cases considered in this work involve measurements only on the ROI around the tumor. Moreover, the measurements are considered available on a mesh much coarser than that used for the estimation of the state vector. Figure 5a shows the mesh used for the evolution model, having noticeable refinement around the tumor. The coarse mesh used for the measurements is shown by Figure 5b. Amplifications of Figures 5a, b around the ROI are presented by Figures 6a, b, respectively. These figures clearly show that the measurements are considered available on a mesh much less refined than that used for the computation of the state variables with the evolution model.

With the hypotheses described above, the state estimation problem with the evolution and observation models given by Eqs. (17a) and (17b), respectively, can be optimally solved with the Kalman filter [10–13, 15]. The recursive equations of the Kalman filter, which require floating point operations of the order  $m^3$  per time step, where  $m$  is the size of the observation vector, are given by [10–13, 15]

$$\hat{\mathbf{x}}_n^- = \mathbf{F}_{n-1} \hat{\mathbf{x}}_{n-1}^+ + \mathbf{s}_n \quad (19a)$$

$$\mathbf{P}_n^- = \mathbf{F}_{n-1} \mathbf{P}_{n-1}^+ \mathbf{F}_{n-1}^T + \mathbf{Q}_n \quad (19b)$$

$$\mathbf{K}_n = \mathbf{P}_n^- \mathbf{H}_n^T [\mathbf{H}_n \mathbf{P}_n^- \mathbf{H}_n^T + \mathbf{R}_n]^{-1} \quad (19c)$$

$$\hat{\mathbf{x}}_n^+ = \hat{\mathbf{x}}_n^- + \mathbf{K}(\mathbf{y}_n - \mathbf{H}_n \hat{\mathbf{x}}_n^-) \quad (19d)$$

$$\mathbf{P}_n^+ = (\mathbf{I} - \mathbf{K}_n \mathbf{H}_n) \mathbf{P}_n^- \quad (19e)$$

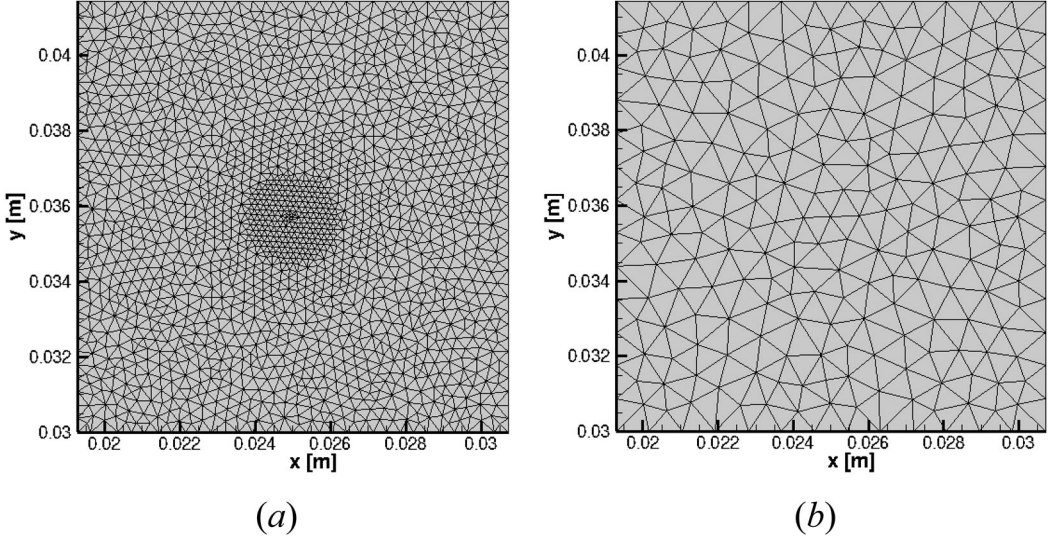


**Figure 6.** Detail of the ROI for (a) state vector and (b) observation vector.

The present state estimation problem involves evolution and observation matrices that are time-invariant. Similarly, by taking into account that the covariance matrices of the evolution and observation noises are constant, we can write:

$$\mathbf{F}_n = \mathbf{F}, \quad \mathbf{H}_n = \mathbf{H}, \quad \mathbf{Q}_n = \mathbf{Q}, \quad \mathbf{R}_n = \mathbf{R} \quad (20)$$

For linear time-invariant systems, the Kalman gain, as well as the prior and posterior error covariance matrices, present an asymptotic behavior [15], that is,

$$\mathbf{P}_n^- \cong \mathbf{P}_n^+ \cong \mathbf{P}_\infty, \quad \mathbf{K}_n \cong \mathbf{K}_\infty \quad (21)$$

In this case, the so-called *Steady-State Kalman Filter* [15] can be used in order to reduce the computational effort to floating point operations of the order  $m^2$  per time step. Although this version of the Kalman filter is not optimal, it has been successfully applied to real-time estimation of the internal temperature with phase-shift measurements [14], as well as to estimation of boundary heat fluxes [16]. The Steady-State Kalman Filter includes the following two equations that are solved only once:

$$\mathbf{P}_\infty = \mathbf{F}\mathbf{P}_\infty\mathbf{F}^T - \mathbf{F}\mathbf{P}_\infty\mathbf{H}^T[\mathbf{H}\mathbf{P}_\infty\mathbf{H}^T + \mathbf{R}]^{-1}\mathbf{H}\mathbf{P}_\infty\mathbf{F}^T + \mathbf{Q} \quad (22a)$$

$$\mathbf{K}_\infty = \mathbf{P}_\infty\mathbf{H}^T[\mathbf{H}\mathbf{P}_\infty\mathbf{H}^T + \mathbf{R}]^{-1} \quad (22b)$$

Eq. (22a) is a Discrete Algebraic Riccati Equation for  $\mathbf{P}_\infty$ , which can be solved with available numerical libraries such as SLICOT [42], which was used in this work. Although the solution of Eq. (22a) is very time consuming, it can be performed offline because it does not depend on the measured data and on the sequentially estimated state variables. With  $\mathbf{K}_\infty$  computed from Eq. (22b), the state variables are then estimated by recursively applying:

$$\hat{\mathbf{x}}_n^+ = [\mathbf{I} - \mathbf{K}_\infty\mathbf{H}]\mathbf{F}\hat{\mathbf{x}}_{n-1}^+ + \mathbf{K}_\infty\mathbf{y}_n \quad (22c)$$

## 5. Results and discussions

For the verification of the Steady-State Kalman Filter, as applied to the solution of the present state estimation problem with state variables and observations given by Eqs. (17a) and (17b),

**Table 1.** Thermal properties of biological tissues [47].

Tissue	$\rho$ [kg m <sup>-3</sup> ]		$c_p$ [J kg <sup>-1</sup> °C <sup>-1</sup> ]		$k$ [W m <sup>-1</sup> °C <sup>-1</sup> ]	
	Mean	Standard deviation	Mean	Standard deviation	Mean	Standard deviation
Dermis/epidermis	1109	14	3391	233	0.37	0.06
Bone/bone marrow	1178	149	2274	234	0.31	0.03
Muscle	1090	52	3421	460	0.49	0.04

**Table 2.** Blood perfusion rate and metabolic heat generation rate [47].

Tissue	$\omega_b/\rho$ [ml min <sup>-1</sup> kg <sup>-1</sup> ]	$g_m/\rho$ [W kg <sup>-1</sup> ]
Dermis/epidermis	106	1.65
Bone/bone marrow	30	0.46
Muscle	37	0.91

respectively, different sets of synthetic measurements were used in this work, obtained with each heating model. For hyperthermia imposed either by the radiofrequency or laser heating, temperature variations were calculated with the solution of the direct problem. In the ROI, these variations were transformed to phase-shift values with Eq. (4), which give the means  $\mathbf{y}_n^{\text{exact}}$  of the Gaussian observations  $\mathbf{y}_n$ , that is

$$\mathbf{y}_n \sim N(\mathbf{y}_n^{\text{exact}}, \mathbf{R}) \quad (23)$$

The observations are assumed to be uncorrelated and with constant standard deviation  $\sigma_{\Delta\Phi} = 0.2^\circ$ . Hence,  $\mathbf{R}$  is given by

$$\mathbf{R} = \sigma_{\Delta\Phi}^2 \mathbf{I} \quad (24)$$

The covariance matrix of the state evolution model,  $\mathbf{Q}$ , was obtained via Monte Carlo simulations, by assuming Gaussian distributions for the thermophysical properties, with means and standard deviations given by Table 1. Uncertainties in other model parameters were not considered in the analysis. The values used in the simulations for the blood perfusion coefficient and for the metabolic heat generation rate are presented in Table 2. The thermal properties in the tumor were assumed to be the same as in the muscle, except for the perfusion coefficient and the metabolic heat generation rate that are expected to be larger due to its increased vascularization. By following references [18, 43–46], we assumed the metabolic heat generation rate to be one order of magnitude larger for the cancerous tissue than for the healthy muscle.

The results obtained with the simulated measurements resulting from the radio frequency and laser heating techniques are presented and discussed next.

### 5.1. Radiofrequency heating

We consider the tumor loaded with  $n = 10^8$  Fe<sub>3</sub>O<sub>4</sub> nanoparticles, with radius  $r = 10^{-8}$  m and  $\chi'' = 18$  [18, 40]. The values of the electrical properties used for the tissues are presented by Table 3, while Table 4 shows the physical properties of the Fe<sub>3</sub>O<sub>4</sub> nanoparticles.

For this case, the electric potential field was calculated with  $u^- = 0$  V and  $u^+ = 10$  V. The exact and the estimated spatial distributions of the temperature variation are presented by Figures 7–9, for times  $t = 20, 40$  and  $60$  s, respectively. These figures show that the temperature variations in the whole region can be accurately estimated, despite the fact that measurements are taken only in the ROI and that large uncertainties are considered in the evolution and observation models. In fact, the estimated spatial distributions of the temperature variation are stable. That is, the inverse problem solution is appropriately regularized by the steady state Kalman filter. An analysis of Figure 9 reveals the temperature variation of  $1.7^\circ\text{C}$  in the tumor, at  $t = 60$  s, due to the

**Table 3.** Electrical properties of tissue at 1 MHz [18, 40, 47].

Tissue	$k_e$ [S m <sup>-1</sup> ]	$\epsilon_r$
Dermis/epidermis	0.0132	991
Bone/bone marrow	0.0904	249
Muscle	0.5030	1840

**Table 4.** Physical properties of Fe<sub>3</sub>O<sub>4</sub> nanoparticles [18, 40].

$\rho$ [kg m <sup>-3</sup> ]	$c_p$ [J kg <sup>-1</sup> °C <sup>-1</sup> ]	$k$ [W m <sup>-1</sup> °C <sup>-1</sup> ]	$k_e$ [S m <sup>-1</sup> ]
5180	4000	40	25000

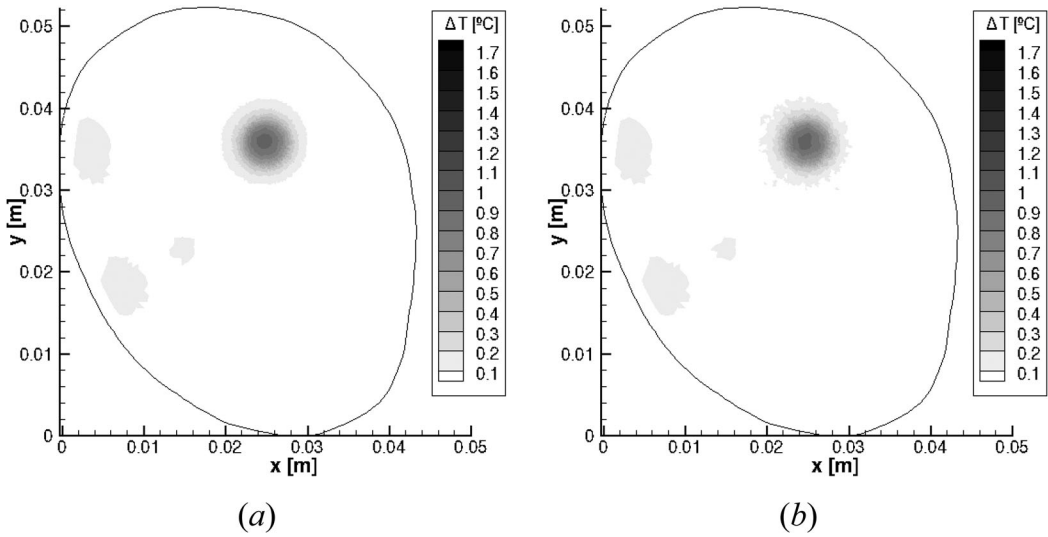


**Figure 7.** Temperature variation with the radiofrequency heating at  $t = 20$  s: (a) exact and (b) estimated.

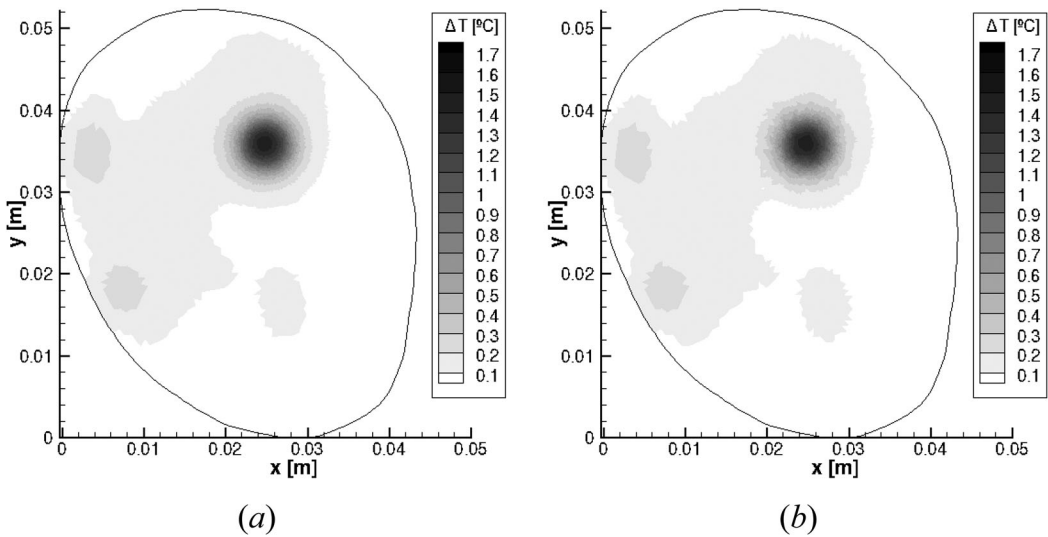


**Figure 8.** Temperature variation with the radiofrequency heating at  $t = 40$  s: (a) exact and (b) estimated.

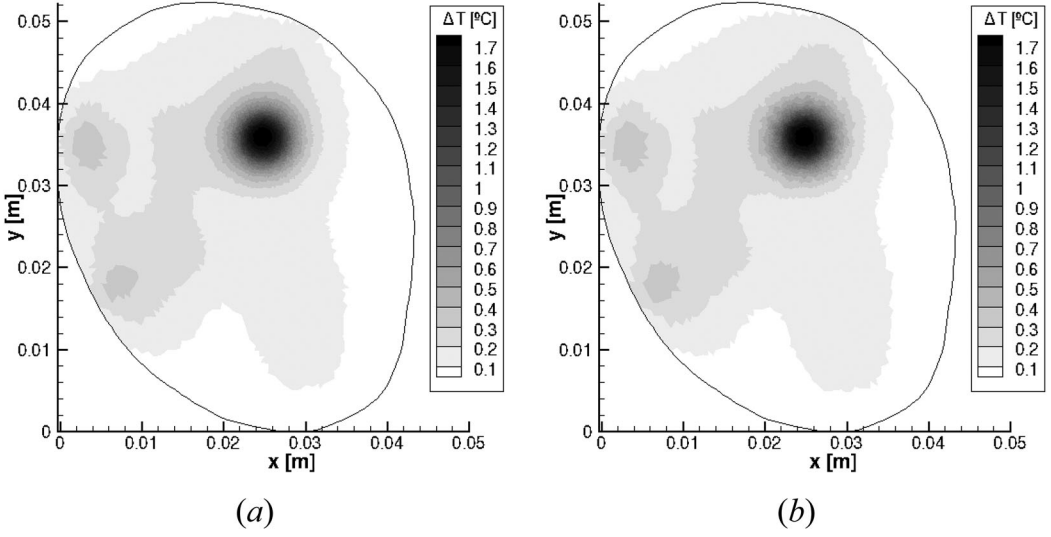


Figure 9. Temperature variation with the radiofrequency heating at  $t = 60$  s: (a) exact and (b) estimated.

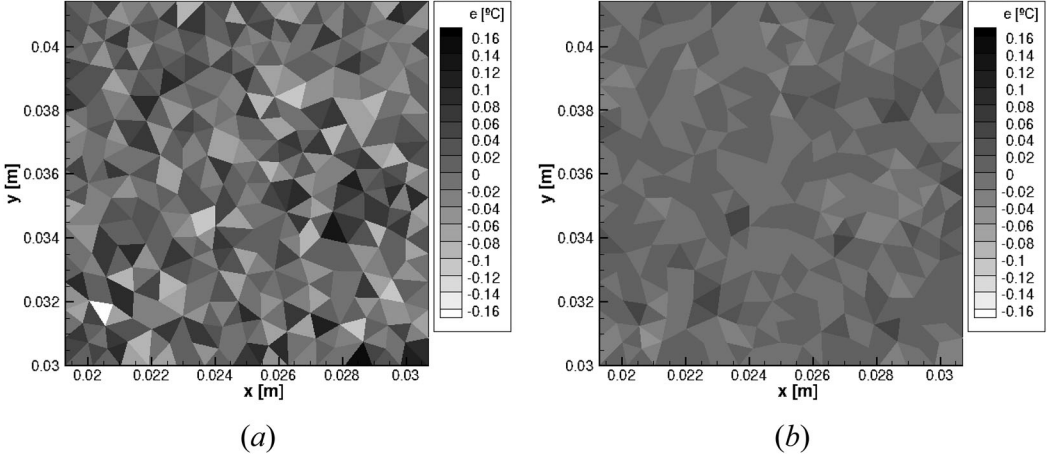


Figure 10. Error between exact and estimated temperature variations with the radio frequency heating at  $t = 20$  s: (a) direct inversion and (b) SSKF.

use of nanoparticles. On the other hand, temperature variations smaller than  $0.5^\circ\text{C}$  are observed outside the ROI, due to the electrical current in the region that does not contain nanoparticles.

We now proceed to compare the estimation errors obtained with the direct inversion of Eq. (4) and with the steady state Kalman filter. Since the direct inversion is only possible at locations where measurements are available, this comparison is focused on the ROI. Figures 10–12 present the estimation errors at  $t = 20, 40$  and  $60$  s, respectively. The errors obtained with the steady state Kalman filter are smaller and smoother than those obtained by direct inversion of the magnetic resonance data. Such is the case because the measurement errors are directly propagated when Eq. (4) is applied to obtain  $\Delta T(\mathbf{r}, t)$ .

A comparison between the synthetic measurements and the phase-shift values predicted with the solution of the state estimation problem is presented in Figures 13–15, for  $t = 20, 40$  and  $60$  s, respectively. As expected, the agreement between measurements and estimated phase-shift values is excellent, resulting in residuals that oscillate around zero and have an order of magnitude



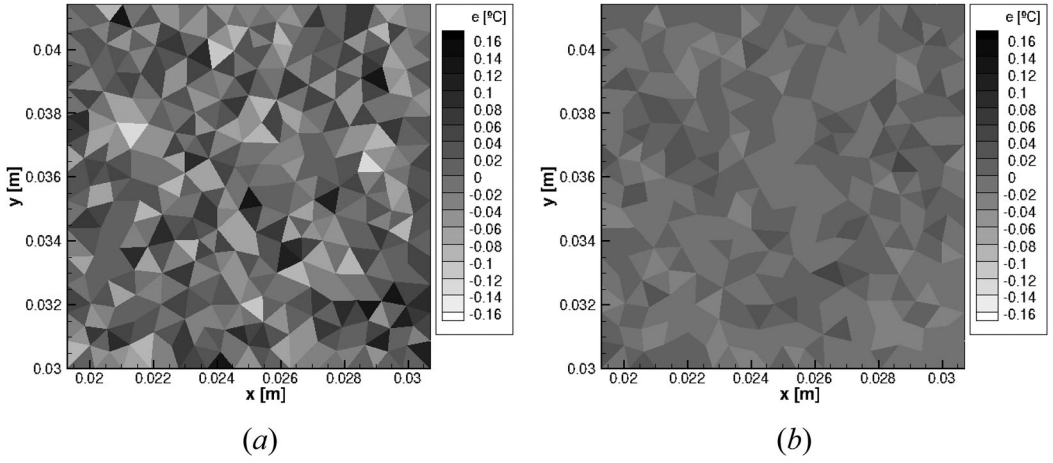


**Figure 11.** Error between exact and estimated temperature variations with the radio frequency heating at  $t = 40$  s: (a) direct inversion and (b) SSKF.

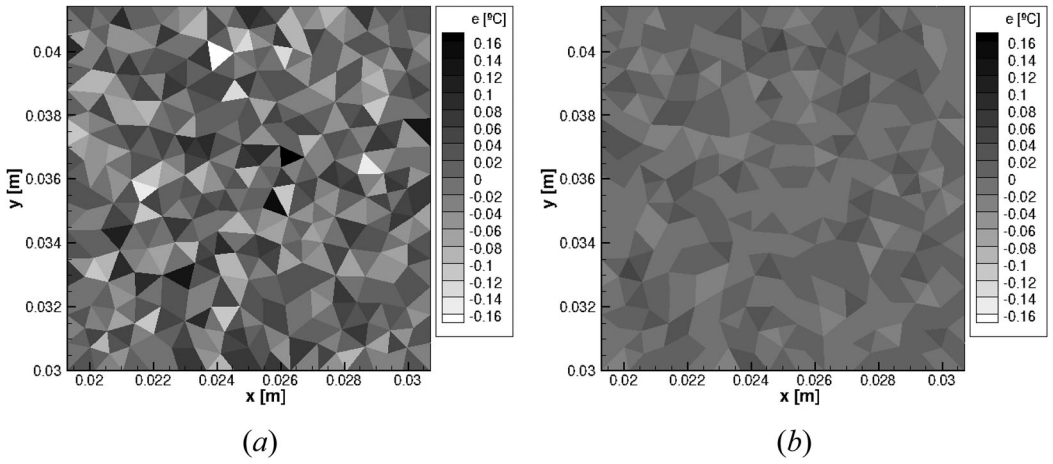


**Figure 12.** Error between exact and estimated temperature variations with the radio frequency heating at  $t = 60$  s: (a) direct inversion and (b) SSKF.

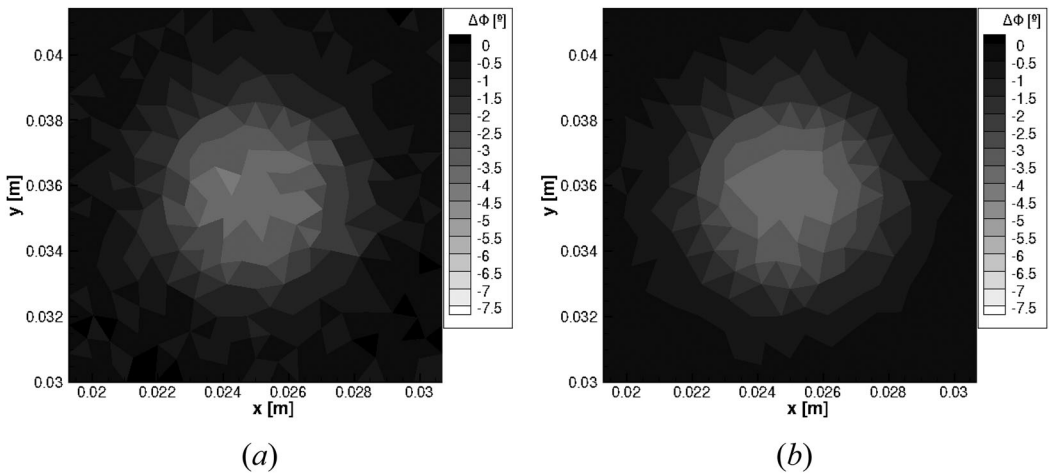


**Figure 13.** Phase-shift with the radio frequency heating at  $t = 20$  s: (a) measurements and (b) estimated with SSKF.

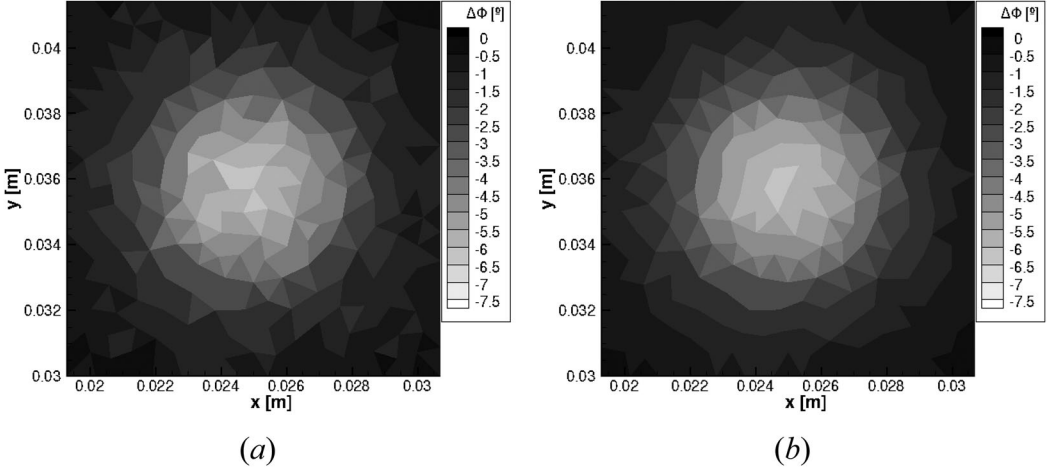


Figure 14. Phase-shift with the radio frequency heating at  $t = 40$  s: (a) measurements and (b) estimated with SSKF.

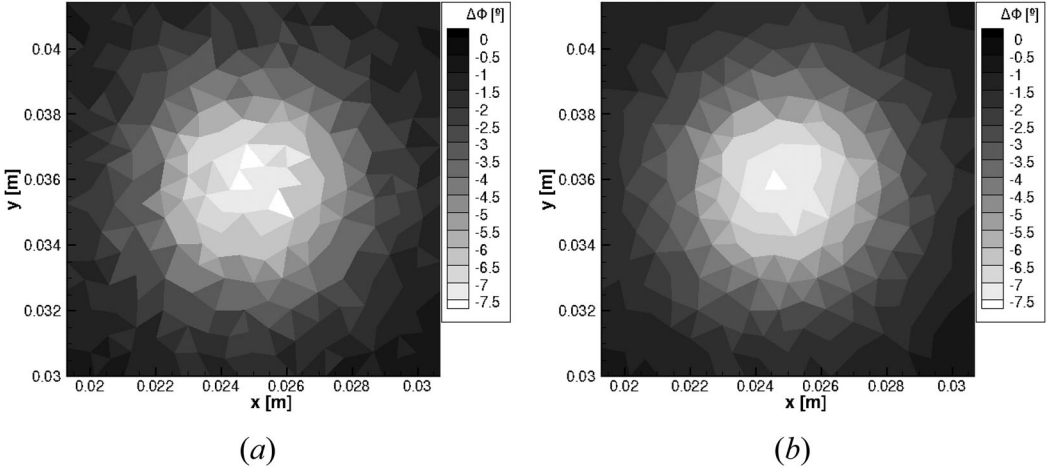


Figure 15. Phase-shift with the radio frequency heating at  $t = 60$  s: (a) measurements and (b) estimated with SSKF.

comparable to the standard deviation for the measurements. The residuals are presented by Figures 16a–c, for the same time instants considered above.

The time evolution of the temperature variation at the center of the tumor region is presented by Figure 17a and the related estimation error by Figure 17b. The simulated measurements are also presented by Figure 17a. These two figures show the more accurate estimates obtained with the steady state Kalman filter than with the direct inversion of Eq. (4). Notice that the solution of the state estimation problem has significantly smaller estimation errors.

An important result of this work is related to the estimation of the actual temperature in the region by using the solution of the state estimation problem, while the direct inversion of Eq. (4) only provides the temperature variation in the region. That is, after solving the state estimation problem, the temperature variation can be combined with the solution of the steady-state bioheat transfer problem for  $T_0(\mathbf{r})$  (see Eq. 5), to obtain  $T(\mathbf{r}, t)$ . The solution of the steady bioheat transfer was performed by means of a Monte Carlo simulation, in order to also account for the uncertainties in the thermophysical properties. These estimated temperatures are compared to the exact ones in Figures 18–20, for  $t = 20$ , 40 and 60 s, respectively. These figures show that accurate



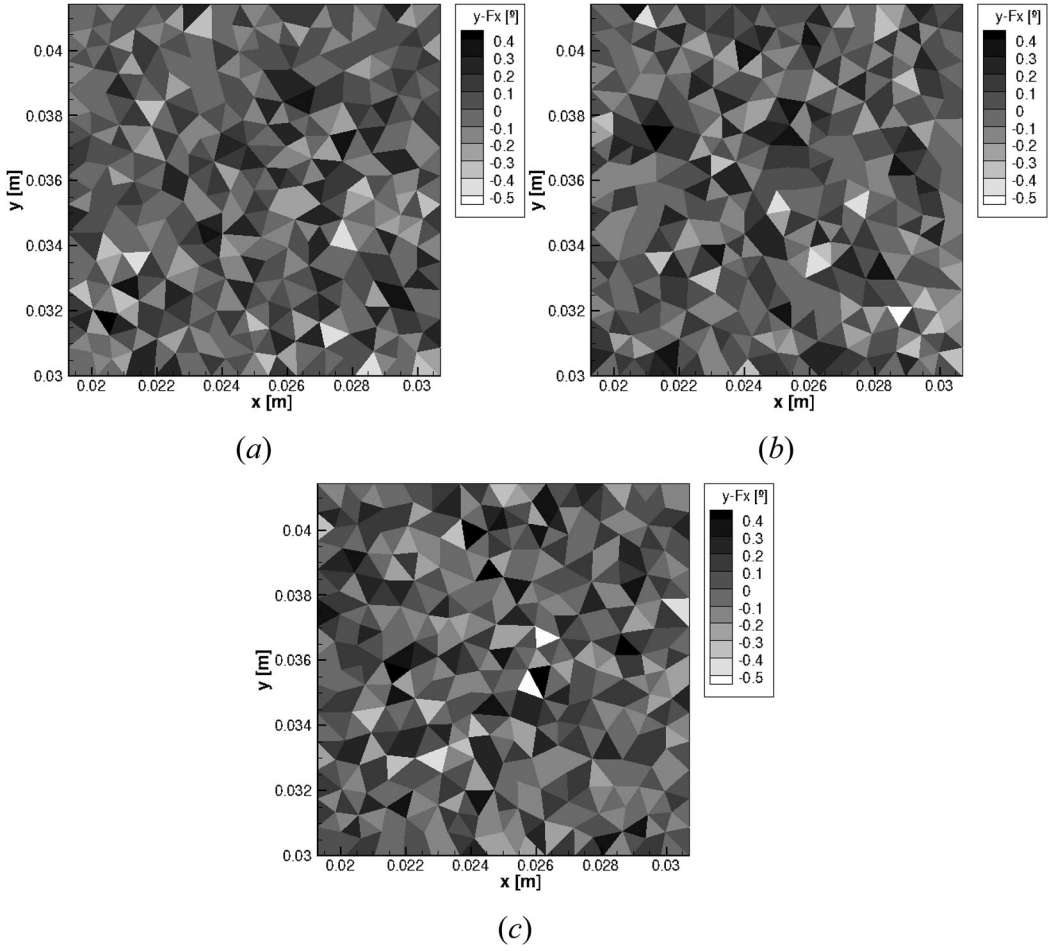


**Figure 16.** Residuals with the radio frequency heating at (a)  $t = 20$  s, (b)  $t = 40$  s, and (c)  $t = 60$  s.

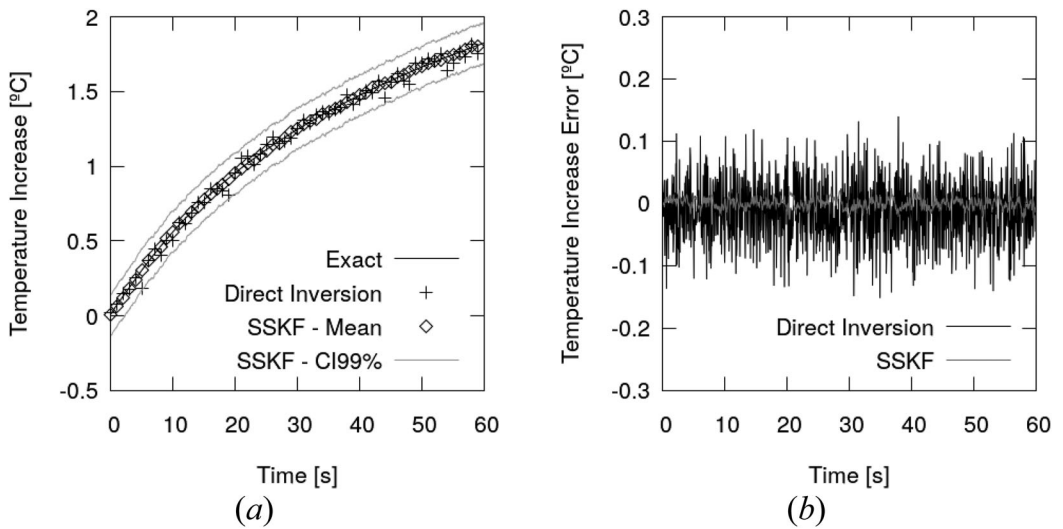


**Figure 17.** Time evolution of the temperature variation at the center of the tumor region (a), and the related estimation error (b), when using radio frequency heating.

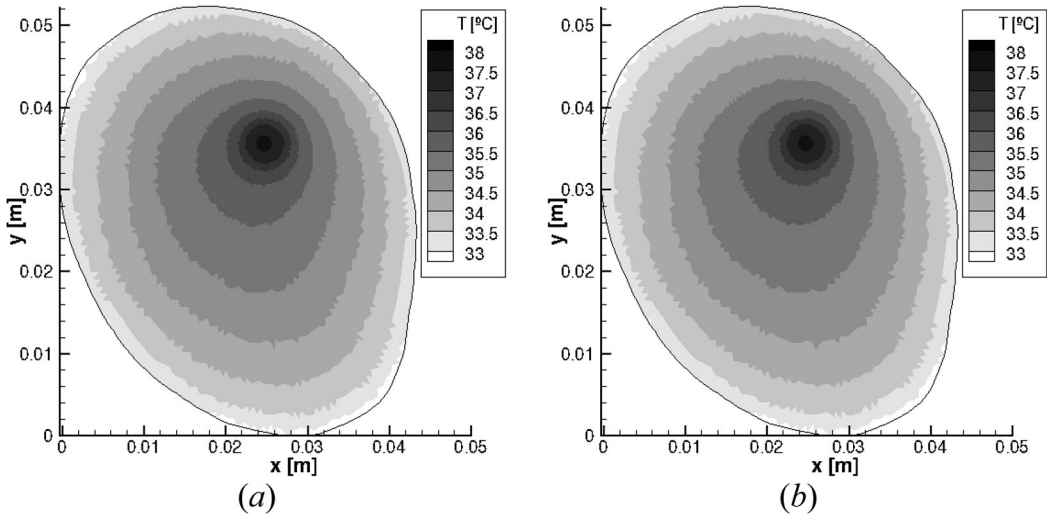


Figure 18. Temperature with the radiofrequency heating at  $t = 20$  s: (a) exact and (b) estimated.

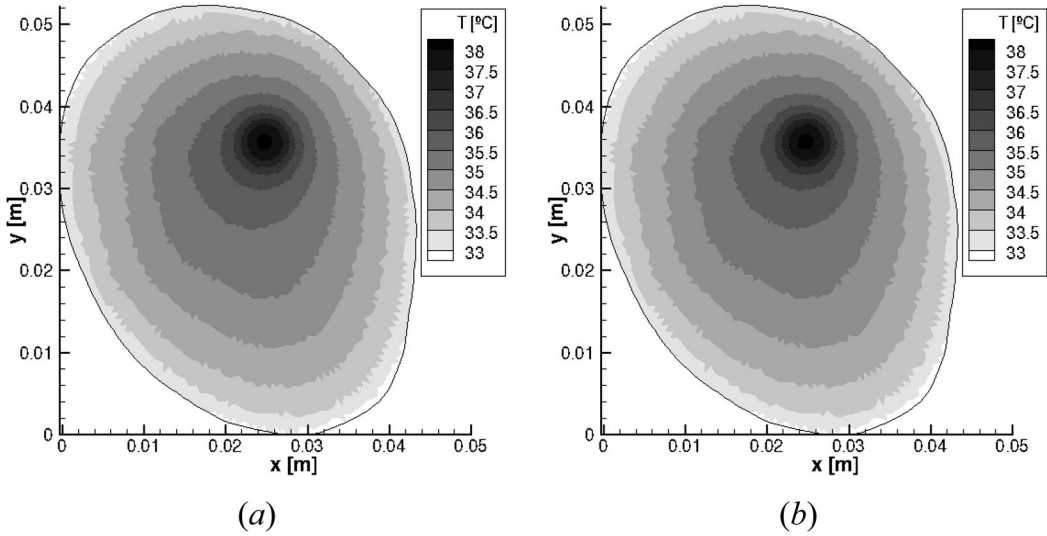


Figure 19. Temperature with the radiofrequency heating at  $t = 40$  s: (a) exact and (b) estimated.

estimates can be obtained for the distribution of the temperature in the region. Similarly, the time variation of the estimated temperature at the center of the tumor region is in excellent agreement with the exact one, as revealed by Figure 21.

## 5.2. Laser-Diode heating

For this case, the laser beam was initially applied at the surface of the skin. However, most of the light was absorbed by the superficial tissues before reaching the ROI, thus, producing no significant heating of the desired region containing the tumor. Therefore, an intrusive heating was considered, with the laser beam applied at the surface of the tumor, along the direction locally normal to the tumor surface, with  $E_0 = 2000 \text{ W m}^{-2}$ . The optical properties assumed for the tissues are shown in Table 5. Deposition of nanoparticles was also considered in this case, by

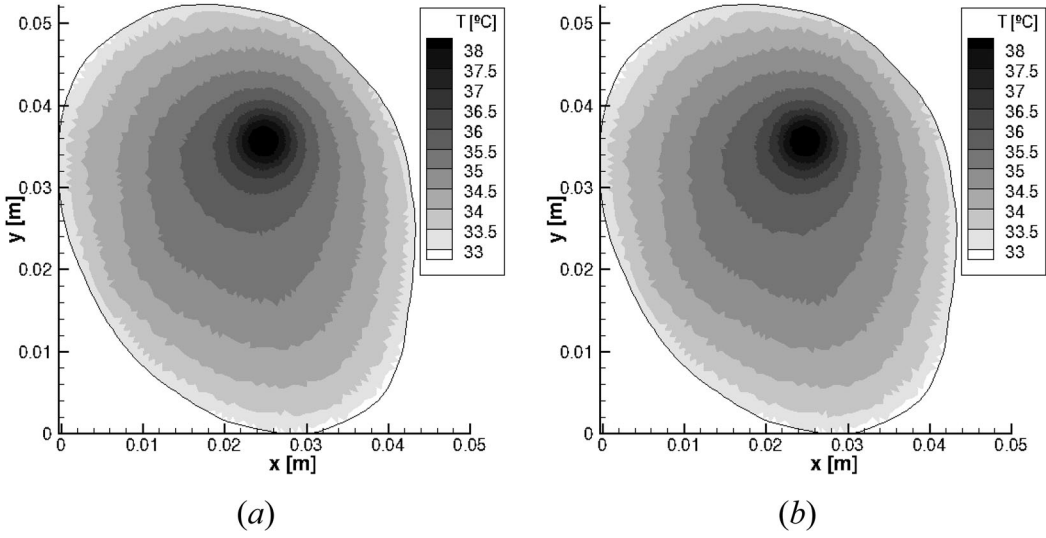


Figure 20. Temperature with the radiofrequency heating at  $t = 60$  s: (a) exact and (b) estimated.

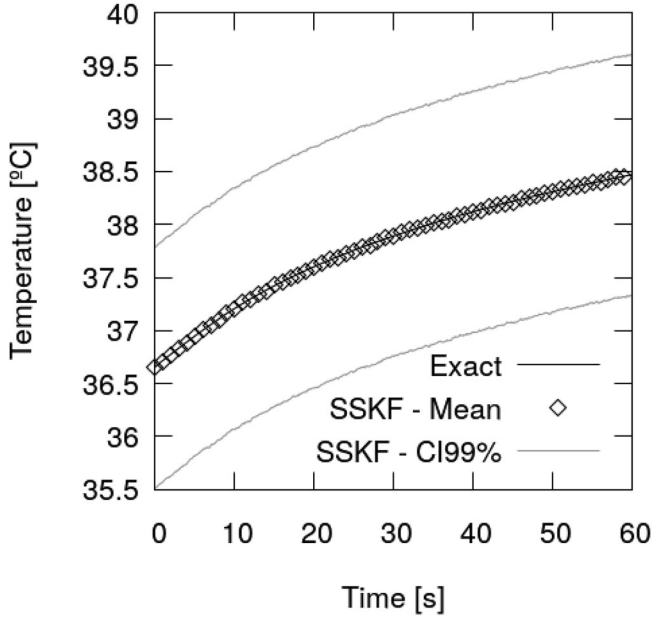


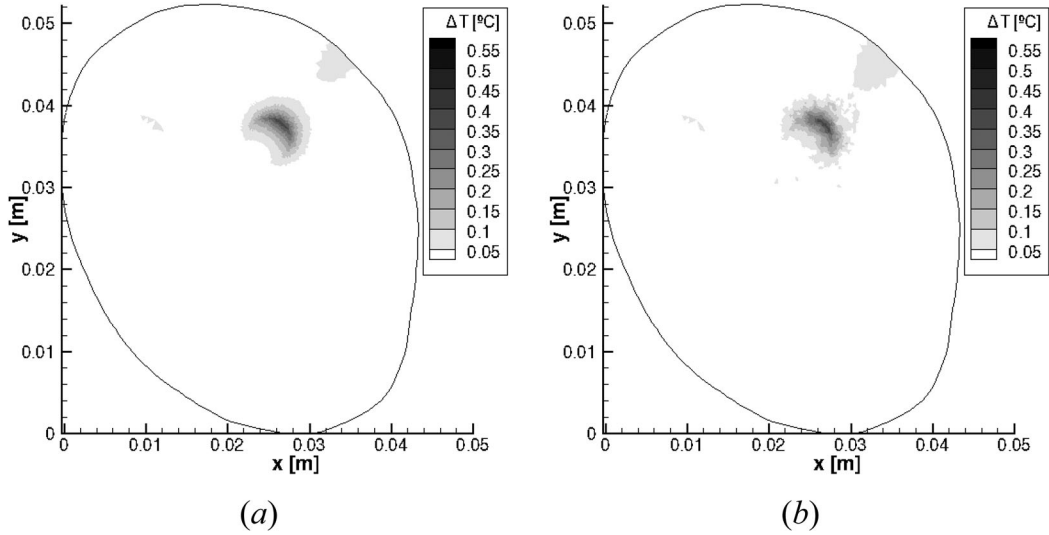
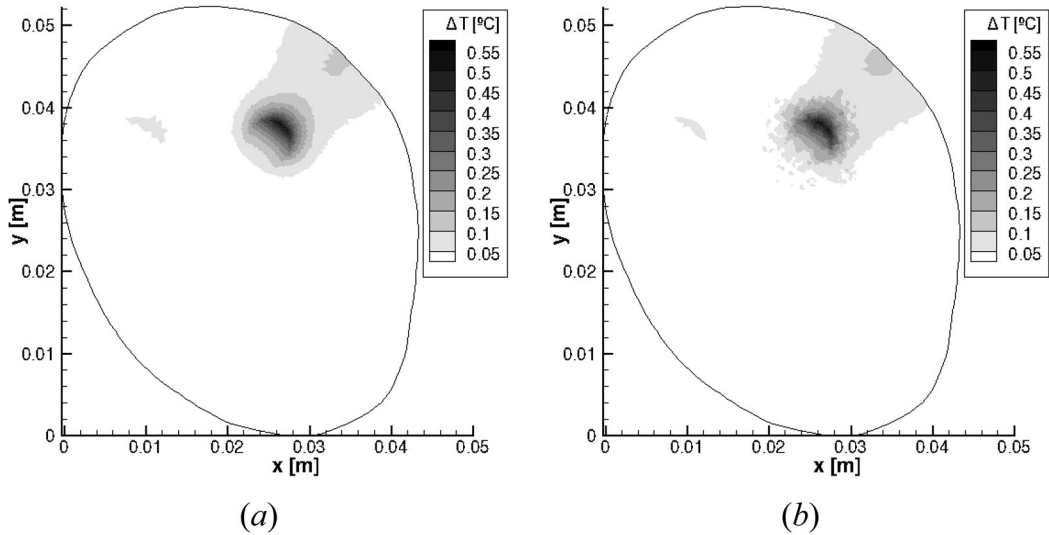
Figure 21. Temperature variation at the center of the tumor region when using radio frequency heating.

assuming the tumor loaded with gold nanorods with effective radius of 11.43 nm at a concentration of  $3 \times 10^{15} \text{ m}^{-3}$ . These gold nanorods were also assumed to affect only the absorption and scattering coefficients, according to Table 5 [23]. The first and second moment of the Fresnel reflection coefficient were assumed to be equal to 0.565 and 0.429, respectively [32].

The exact and estimated spatial distributions of the temperature variations (obtained with the steady state Kalman filter) are presented in Figures 22–24, for  $t = 20, 40$  and  $60$  s, respectively. Similarly as in the case of the radio frequency heating, the agreement between estimated and exact temperature variations when using laser diode heating is excellent. However, we point out that the heating pattern in this case differs from that obtained with the radio frequency heating

**Table 5.** Optical properties of tissues [23, 41].

Tissue	$\kappa$ [ $\text{m}^{-1}$ ]	$\zeta_s$ [ $\text{m}^{-1}$ ]	$f_a$
Dermis/epidermis	122	22500	0.9
Bone/bone marrow	54	6670	0.9
Muscle	54	6670	0.93
Tumor with gold nanorods	188.38	22505.19	0.93

**Figure 22.** Temperature variation with the laser heating at  $t = 20$  s: (a) exact and (b) estimated.**Figure 23.** Temperature variation with the laser heating at  $t = 40$  s: (a) exact and (b) estimated.

(see also Figures 7–9). While the heating of the tumor was quite uniform with the radio frequency external electrodes, the laser heating follows the attenuation of the light intensity along its main direction of propagation in the tissues. Therefore, as can be noticed in Figures 22–24, the heating of the tumor region with the laser is nonuniform.

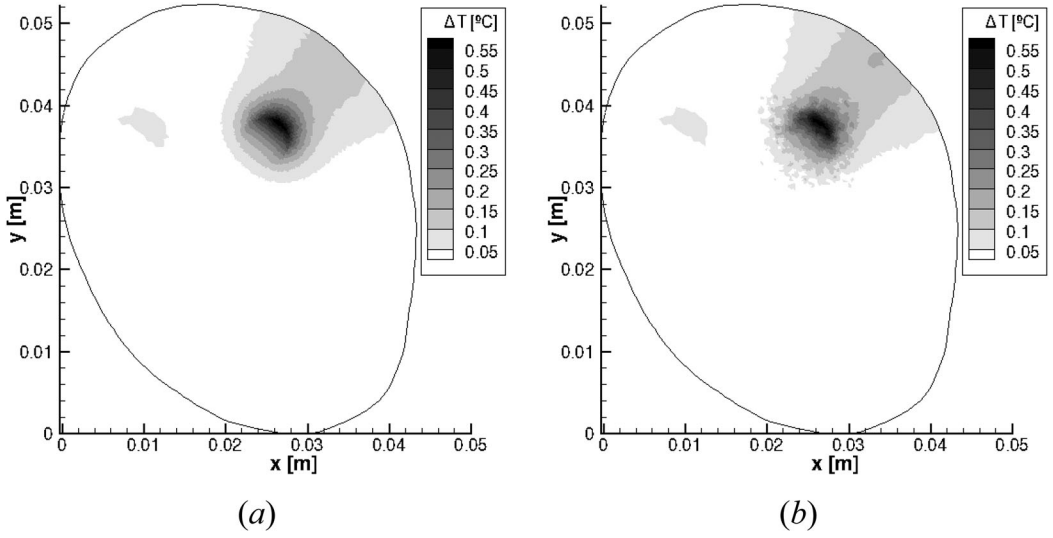


**Figure 24.** Temperature variation with the laser heating at  $t = 60$  s: (a) exact and (b) estimated.

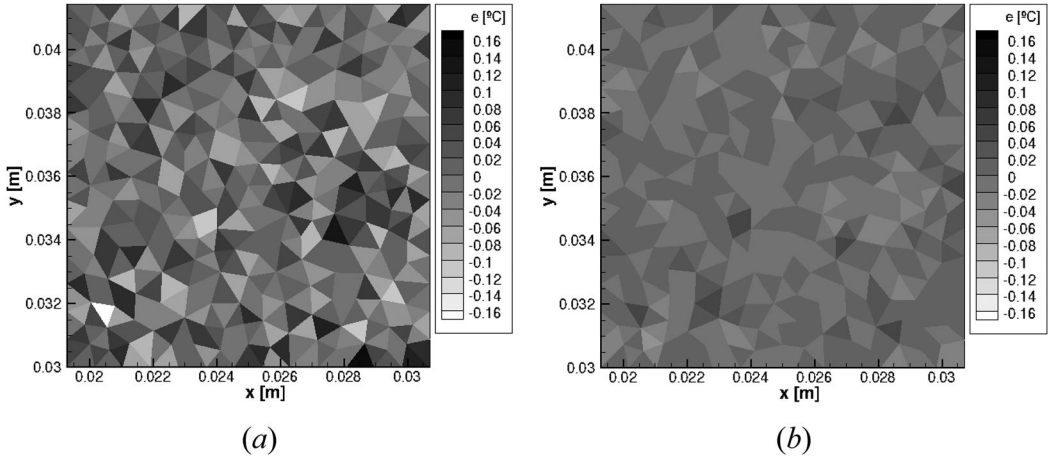


**Figure 25.** Error between exact and estimated temperature variations with the laser heating at  $t = 60$  s: (a) direct inversion and (b) SSKF.

Other results obtained for the case with laser heating are similar to those obtained with the radiofrequency heating and are summarized below for the sake of brevity. A comparison of the estimation errors of the temperature variations in the ROI, obtained with the direct inversion and with the solution of the state estimation problem, are presented in [Figure 25](#), for  $t = 60$  s. This figure shows that the magnitude of the estimation errors obtained with the steady state Kalman filter are much smaller than those for the direct inversion. Moreover, the estimation errors for the direct inversion are quite oscillatory, because measurement errors are directly propagated to the estimated temperature variations obtained with [Eq. \(4\)](#). Such behavior can also be observed with the time variation of the estimation error at the center of the tumor region, which is presented in [Figure 26](#).

A comparison between the synthetic measurements and the phase-shift values in the ROI, estimated with the steady state Kalman filter, is shown by [Figure 27](#), for  $t = 60$  s. As in the previous case, the estimated phase-shift distribution is smoother than the measurements, but still keeps the

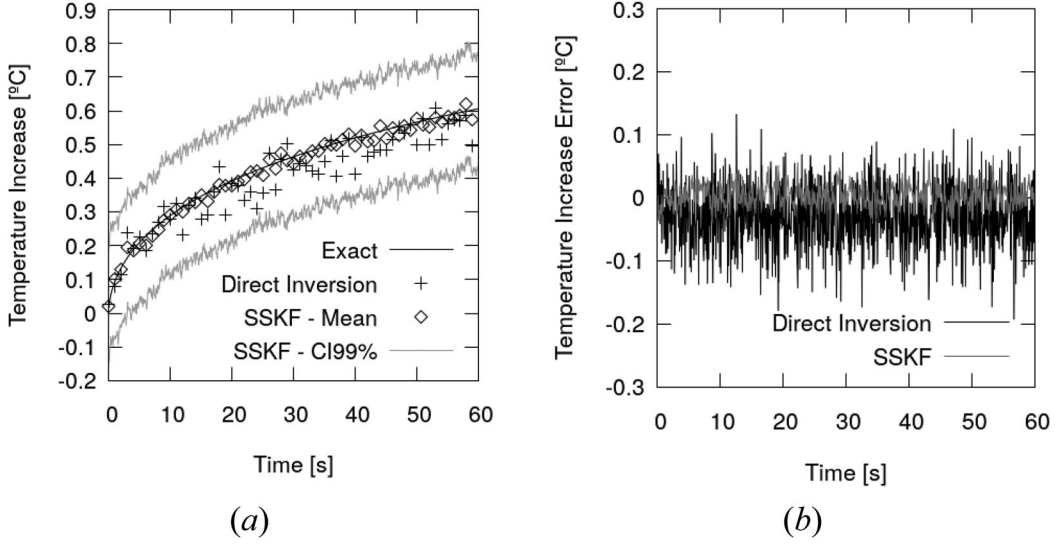


Figure 26. Time evolution of the estimation error at the center of the tumor region with the laser heating.

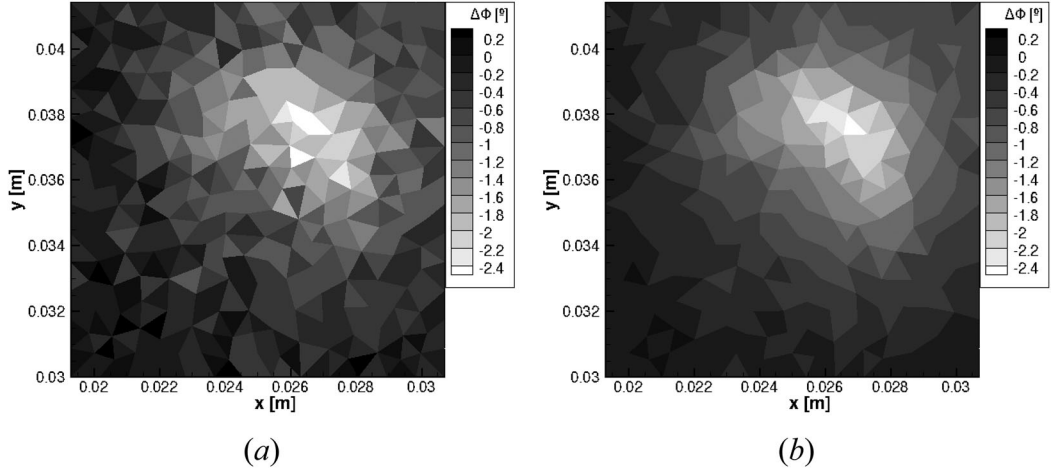
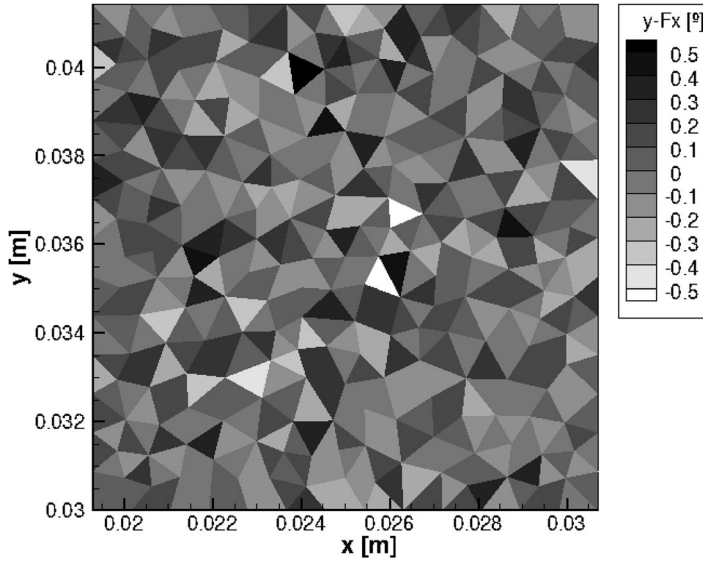


Figure 27. Phase-shift with the laser heating at  $t = 60$  s: (a) measurements and (b) estimated with SSKF.

same qualitative behavior due to the influence of the likelihood function in the solution of the state estimation problem. As a result, the residuals oscillate around zero, with the same order of magnitude of the standard deviation of the measurements, as shown in Figure 28 for the ROI. The temperatures obtained with the temperature variations estimated with the steady state Kalman filter are also in excellent agreement with the exact ones for the laser heating, as shown by Figures 29a, b, at  $t = 60$  s.

Numerical simulations were performed on an Intel® Core™ i7-2600@3.40 GHz computer, with 16 GB of RAM, running a 64-bit Linux operating system. Computer codes were developed in FORTRAN90 language and the *gfortran* compiler was utilized. Parallelization of the recursive process was performed with OpenMP on 8 threads. The numerical grid, obtained with the Gmsh software [37], involved 10798 grid cells and resulted in a dense  $F$  matrix. As for the preprocessing step, the Discrete Algebraic Riccati Eq. (22a) was solved using the SLICOT numerical library [42], with computational times between 10 and 14 hours. The recursive estimation process with the steady state Kalman filter required 45 seconds of computational time, which is well below the





**Figure 28.** Residuals with the radio frequency heating at  $t = 60$  s.

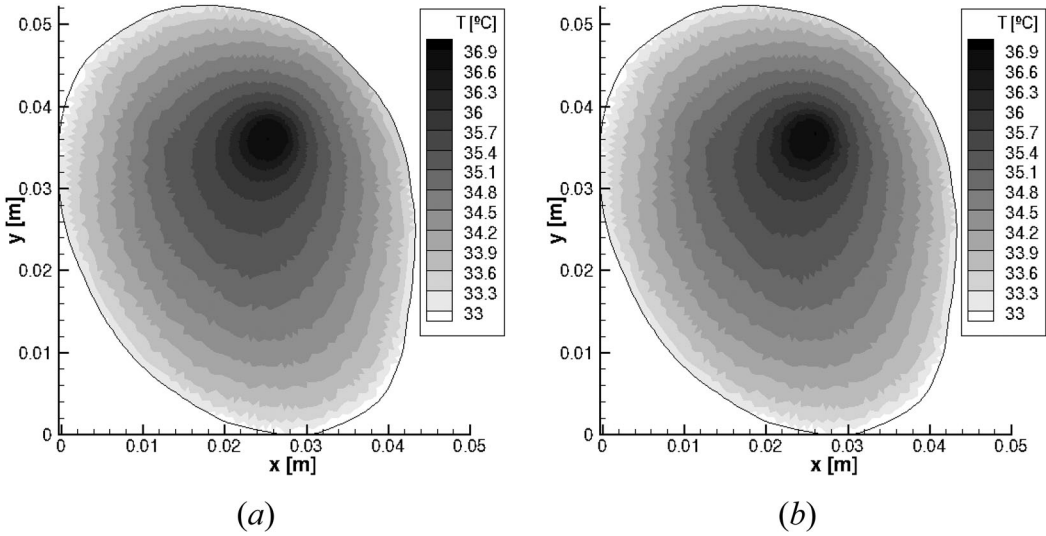


**Figure 29.** Temperature with the laser heating at  $t = 60$  s: (a) exact and (b) estimated.

physical time of 60 seconds considered in this work. Therefore, the temperature in the region can be estimated in real time, since the preprocessing step can be performed offline, that is, before the estimation procedure.

## 6. Conclusions

The objective of this work was the estimation of the unsteady temperature field in a two-dimensional domain, during the hyperthermia treatment of cancer. The phase shift magnetic resonance thermometry technique was rewritten as a state estimation problem and solved with the Steady State Kalman Filter algorithm. The evolution model consisted of Pennes' equation for bioheat

transfer, coupled with either an electrical model for the radio frequency heating or a diffusion approximation for the light propagation in the tissues with laser heating. This work specifically examined the use of measurements only in the Region of Interest that includes the tumor, where the largest temperature increases take place during the hyperthermia treatment. In addition, the local phase shift measurements were considered available on a mesh coarser than that used for the solution of the state estimation problem. The tumor was considered loaded with nanoparticles in order to improve the localized heating during the hyperthermia treatment and avoid thermal damage to surrounding healthy cells.

The numerical simulations resulted in a uniform temperature increase inside the tumor, when the heating with radio frequency was applied. On the other hand, the laser was strongly attenuated by the tissues along its main direction of propagation, thus, resulting in nonuniform temperature increase of the tumor, even with intrusive heating. Results obtained with simulated measurements revealed that the Steady State Kalman Filter provided stable and accurate estimations for the temperature in the whole region, despite the fact that the measurements were only considered on a coarse mesh in the Region of Interest. Moreover, the solution of the state estimation problem resulted in smaller and smoother estimation errors than the direct inversion of the magnetic resonance data, for both heating techniques examined in this work. The solution of the state estimation problem with the Steady State Kalman Filter was faster than the physical duration of the simulated hyperthermia treatment. Therefore, the present solution procedure permits the real-time estimation of the temperature field in regions undergoing a hyperthermia treatment for cancer, with results more accurate than the direct inversion of the magnetic resonance data.

## Disclosure statement

There are no relationships of any of the authors of this article with any people or organizations that could inappropriately influence (bias) this work.

## Funding

This work was supported by Conselho Nacional de Desenvolvimento Científico e Tecnológico (CNPq), Coordenação de Aperfeiçoamento de Pessoal de Nível Superior (CAPES), Fundação Carlos Chagas Filho de Amparo a Pesquisa do Estado do Rio de Janeiro (FAPERJ), Programa de Recursos Humanos da Agência Nacional de Óleo, Gás Natural e Biocombustíveis [ANP/PRH37] and DGI of Universidad Santiago de Cali, Colombia, project No. 819-621118-120.

## ORCID

César C. Pacheco  <http://orcid.org/0000-0003-4935-8655>  
 Helcio R. B. Orlande  <http://orcid.org/0000-0002-3511-322X>  
 Marcelo J. Colaço  <http://orcid.org/0000-0002-8020-6222>  
 George S. Dulikravich  <http://orcid.org/0000-0003-3292-2723>  
 Leonardo A. B. Varón  <http://orcid.org/0000-0002-8078-716X>  
 Bernard Lamien  <http://orcid.org/0000-0003-1665-2620>

## References

- [1] K. Hynynen, W. R. Freund, H. E. Cline, A. H. Chung, R. D. Watkins, J. P. Vetro, and F. A. Jolesz, "A clinical, noninvasive, MR imaging-monitored ultrasound surgery method," *RadioGraphics*, vol. 16, no. 1, pp. 185–195, Jan. 1996. DOI: [10.1148/radiographics.16.1.185](https://doi.org/10.1148/radiographics.16.1.185).
- [2] V. Rieke and K. Butts Pauly, "MR thermometry," *J. Magn. Reson. Imaging*, vol. 27, no. 2, pp. 376–390, Feb. 2008. DOI: [10.1002/jmri.21265](https://doi.org/10.1002/jmri.21265).



- [3] B. R. Loiola, H. R. B. Orlande, and G. S. Dulikravich, "Thermal damage during ablation of biological tissues," *Numer. Heat Transf. Part A Appl.*, vol. 73, no. 10, pp. 685–701, 2018. DOI: [10.1080/10407782.2018.1464794](https://doi.org/10.1080/10407782.2018.1464794).
- [4] Y. Bayazitoglu, "Nanoshell-assisted cancer thermal therapy: numerical simulations," presented at the Proc 2nd ASME Micro/Nanoscale Heat & Mass Transfer: An International Conference, Shanghai, 2009.
- [5] Y. Bayazitoglu, S. Kheradmand, and T. K. Tullius, "An overview of nanoparticle assisted laser therapy," *Int. J. Heat Mass Transf.*, vol. 67, pp. 469–486, Dec. 2013. DOI: [10.1016/j.ijheatmasstransfer.2013.08.018](https://doi.org/10.1016/j.ijheatmasstransfer.2013.08.018).
- [6] L. A. Dombrovsky, V. Timchenko, M. Jackson, and G. H. Yeoh, "A combined transient thermal model for laser hyperthermia of tumors with embedded gold nanoshells," *Int. J. Heat Mass Transf.*, vol. 54, no. 25–26, pp. 5459–5469, Dec. 2011. DOI: [10.1016/j.ijheatmasstransfer.2011.07.045](https://doi.org/10.1016/j.ijheatmasstransfer.2011.07.045).
- [7] L. A. Dombrovsky, V. Timchenko, C. Pathak, H. Piazena, W. Müller, and M. Jackson, "Radiative heating of superficial human tissues with the use of water-filtered infrared-A radiation: a computational modeling," *Int. J. Heat Mass Transf.*, vol. 85, pp. 311–320, 2015. DOI: [10.1016/j.ijheatmasstransfer.2015.01.133](https://doi.org/10.1016/j.ijheatmasstransfer.2015.01.133).
- [8] B. Denis de Senneville, B. Quesson, and C. T. W. Moonen, "Magnetic resonance temperature imaging," *Int. J. Hyperthermia*, vol. 21, no. 6, pp. 515–531, 2005. DOI: [10.1080/02656730500133785](https://doi.org/10.1080/02656730500133785).
- [9] Y. Ishihara, Y. Ishihara, A. Calderon, H. Watanabe, K. Okamoto, Y. Suzuki, K. Kuroda, and Y. Suzuki, "A precise and fast temperature mapping using water proton chemical shift," *Magn. Reson. Med.*, vol. 34, no. 6, pp. 814–823, 1995. DOI: [10.1002/mrm.1910340606](https://doi.org/10.1002/mrm.1910340606).
- [10] J. P. Kaipio and E. Somersalo, *Statistical and Computational Inverse Problems*. New York, NY: Springer Science + Business Media, Inc, 2004.
- [11] H. R. B. Orlande, M. Colaço, G. Dulikravich, F. Vianna, W. da Silva, H. Fonseca, and O. Fudym, "State estimation problems in heat transfer," *Int. J. Uncertain. Quantif.*, vol. 2, no. 3, pp. 239–258, 2012. DOI: [10.1615/Int.J.UncertaintyQuantification.2012003582](https://doi.org/10.1615/Int.J.UncertaintyQuantification.2012003582).
- [12] A. Doucet, A. Smith, N. de Freitas, and N. Gordon, *Sequential Monte Carlo Methods in Practice*. New York: Springer, 2001.
- [13] M. S. Arulampalam, S. Maskell, N. Gordon, and T. Clapp, "A tutorial on particle filters for online nonlinear/non-Gaussian Bayesian tracking," *IEEE Trans. Signal Process.*, vol. 50, no. 2, pp. 174–188, 2002. DOI: [10.1109/78.978374](https://doi.org/10.1109/78.978374).
- [14] C. Pacheco, H. R. B. Orlande, M. J. Colaço, and G. S. Dulikravich, "State estimation problems in PRF-shift magnetic resonance thermometry," *Int. J. Numer. Methods Heat Fluid Flow*, vol. 28, no. 2, pp. 315–335, Jan. 2018. DOI: [10.1108/HFF-10-2016-0427](https://doi.org/10.1108/HFF-10-2016-0427).
- [15] D. Simon, *Optimal State Estimation: Kalman, H Infinity, and Nonlinear Approaches*. New Jersey, USA: John Wiley & Sons, Inc., 2006.
- [16] C. C. Pacheco, H. R. B. Orlande, M. J. Colaço, and G. S. Dulikravich, "Real-time identification of a high-magnitude boundary heat flux on a plate," *Inverse Probl. Sci. Eng.*, vol. 24, no. 9, pp. 1661–1679, 2016. DOI: [10.1080/17415977.2016.1195829](https://doi.org/10.1080/17415977.2016.1195829).
- [17] P. Gas and A. Miaskowski, "Specifying the ferrofluid parameters important from the viewpoint of magnetic fluid hyperthermia," presented at the 2015 Selected Problems of Electrical Engineering and Electronics (WZEE), Kielce, Poland, 2015, pp. 1–6, DOI: [10.1109/WZEE.2015.7394040](https://doi.org/10.1109/WZEE.2015.7394040). [[10.1109/WZEE.2015.7394040](https://doi.org/10.1109/WZEE.2015.7394040)]
- [18] L. A. B. Varon, H. R. B. Orlande, and G. E. Eliçabe, "Estimation of state variables in the hyperthermia therapy of cancer with heating imposed by radiofrequency electromagnetic waves," *Int. J. Therm. Sci.*, vol. 98, pp. 228–236, 2015. DOI: [10.1016/j.ijthermalsci.2015.06.022](https://doi.org/10.1016/j.ijthermalsci.2015.06.022).
- [19] P. Gas, "Temperature inside tumor as time function in RF hyperthermia," *Przegląd Elektrotechniczny*, vol. 86, pp. 42–45, 2010.
- [20] R. Goyal and K. Vafai, "Electromagnetic field-induced thermal management of biological materials," *Numer. Heat Transf. Part Appl.*, vol. 72, no. 4, pp. 275–290, Aug. 2017. DOI: [10.1080/10407782.2017.1372672](https://doi.org/10.1080/10407782.2017.1372672).
- [21] E. Kurgan and P. Gas, "Analysis of electromagnetic heating in magnetic fluid deep hyperthermia," presented at the 2016 17th International Conference Computational Problems of Electrical Engineering (CPEE), IEEE Xplore, Sandomierz, Poland, pp. 1–4, Sep. 14–17, 2016. DOI: [10.1109/CPEE.2016.7738756](https://doi.org/10.1109/CPEE.2016.7738756). [[10.1109/CPEE.2016.7738756](https://doi.org/10.1109/CPEE.2016.7738756)]
- [22] L. A. B. Varon, H. R. B. Orlande, and G. E. Eliçabe, "Combined parameter and state estimation problem in a complex domain: Rf hyperthermia treatment using nanoparticles," *J. Phys. Conf. Series (Print)*, vol. 745, pp. 032014, 2016. DOI: [10.1088/1742-6596/745/3/032014](https://doi.org/10.1088/1742-6596/745/3/032014).
- [23] B. Lamien, H. R. B. Orlande, and G. E. Eliçabe, "Inverse problem in the hyperthermia therapy of cancer with laser heating and plasmonic nanoparticles," *Inverse Probl. Sci. Eng.*, vol. 25, no. 4, pp. 608–631, May 2016. DOI: [10.1080/17415977.2016.1178260](https://doi.org/10.1080/17415977.2016.1178260).
- [24] N. Afrin and Y. Zhang, "Uncertainty analysis of thermal damage to living biological tissues by laser irradiation based on a generalized dual-phase lag model," *Numer. Heat Transf. Part A Appl.*, vol. 71, no. 7, pp. 693–706, Apr. 2017. DOI: [10.1080/10407782.2017.1308714](https://doi.org/10.1080/10407782.2017.1308714).

- [25] H. Nirgudkar, S. Kumar, and A. Srivastava, "Thermal analysis of laser-irradiated tissue phantoms using a novel separation of the variables-based discrete transfer method," *Numer. Heat Transf. Part A Appl.*, vol. 71, no. 5, pp. 575–589, Mar. 2017. DOI: [10.1080/10407782.2016.1277925](https://doi.org/10.1080/10407782.2016.1277925).
- [26] B. Lamien, H. R. B. Orlande, L. A. B. Varon, R. L. Q. Basto, G. E. Elicabe, D. S. dos Santos, and R. M. Cotta, "Estimation of the temperature field in laser-induced hyperthermia experiments with a phantom," *Int. J. Hyperthermia*, vol. 35, no. 1, pp. 279–290, 2018. DOI: [10.1080/02656736.2018.1496283](https://doi.org/10.1080/02656736.2018.1496283).
- [27] W. G. Schneider, H. J. Bernstein, and J. A. Pople, "Proton magnetic resonance chemical shift of free (gaseous) and associated (liquid) hydride molecules," *J. Chem. Phys.*, vol. 28, no. 4, pp. 601–601, 1958. DOI: [10.1063/1.1744199](https://doi.org/10.1063/1.1744199).
- [28] D. L. Parker, V. Smith, P. Sheldon, L. E. Crooks, and L. Fussell, "Temperature distribution measurements in two-dimensional NMR imaging," *Med. Phys.*, vol. 10, no. 3, pp. 321–321, 1983. DOI: [10.1118/1.595307](https://doi.org/10.1118/1.595307).
- [29] D. L. Bihan, J. Delannoy, and R. L. Levin, "Temperature mapping with MR imaging of molecular diffusion: Application to hyperthermia," *Radiology*, vol. 171, no. 3, pp. 853–857, Jun. 1989. DOI: [10.1148/radiology.171.3.2717764](https://doi.org/10.1148/radiology.171.3.2717764).
- [30] J. A. De Zwart, P. Van Gelderen, D. J. Kelly, and C. T. Moonen, "Fast magnetic-resonance temperature imaging," *J. Magn. Reson.*, vol. 112, no. 1, pp. 86–90, 1996. DOI: [10.1006/jmrb.1996.0115](https://doi.org/10.1006/jmrb.1996.0115).
- [31] D. J. Griffiths, *Introduction to Electrodynamics*. New Jersey, USA: Prentice Hall, 1999.
- [32] R. W. Brown, Y. N. Cheng, E. M. Haacke, M. R. Thompson, and R. Venkatesan, *Magnetic Resonance Imaging: Physical Principles and Sequence Design*. New Jersey, USA: Wiley, 1999.
- [33] V. Kuperman, *Magnetic Resonance Imaging: Physical Principles and Applications*. San Diego, CA: Elsevier Science, 2000.
- [34] H. H. Pennes, "Analysis of tissue and arterial blood temperatures in the resting human forearm," *J. Appl. Physiol.*, vol. 1, no. 2, pp. 93–122, Aug. 1948. DOI: [10.1152/jappl.1948.1.2.93](https://doi.org/10.1152/jappl.1948.1.2.93).
- [35] M. J. Ackerman, "The Visible Human Project," *Proc. IEEE*, vol. 86, no. 3, pp. 504–511, 1998. DOI: [10.1109/5.662875](https://doi.org/10.1109/5.662875).
- [36] V. M. Spitzer and D. G. Whitlock, "The visible human dataset: the anatomical platform for human simulation," *Anat. Rec.*, vol. 253, no. 2, pp. 49–57, 1998. DOI: [10.1002/\(SICI\)1097-0185\(199804\)253:2<49::AID-AR8>3.0.CO;2-9](https://doi.org/10.1002/(SICI)1097-0185(199804)253:2<49::AID-AR8>3.0.CO;2-9).
- [37] C. Geuzaine and J.-F. Remacle, "Gmsh: A 3-D finite element mesh generator with built-in pre- and post-processing facilities," *Int. J. Numer. Methods Eng.*, vol. 79, no. 11, pp. 1309–1331, Sep. 2009. DOI: [10.1002/nme.2579](https://doi.org/10.1002/nme.2579).
- [38] H. K. Versteeg and W. Malalasekera, *An Introduction to Computational Fluid Dynamics: The Finite Volume Method*. Harlow, Essex, UK: Longman Group Ltd, 1995.
- [39] S. R. Mathur and J. Y. Murthy, "A pressure-based method for unstructured meshes," *Numer. Heat Transf. Part B Fundam.*, vol. 31, no. 2, pp. 195–215, 1997. DOI: [10.1080/10407799708915105](https://doi.org/10.1080/10407799708915105).
- [40] L. A. B. Varon, H. R. B. Orlande, and G. E. Elicabe, "Combined parameter and state estimation in the radio frequency hyperthermia treatment of cancer," *Numer. Heat Transf. Part A Appl.*, vol. 70, no. 6, pp. 581–594, 2016. Sep. DOI: [10.1080/10407782.2016.1193342](https://doi.org/10.1080/10407782.2016.1193342).
- [41] B. Lamien, L. A. B. Varon, H. R. B. Orlande, and G. E. Elicabe, "State estimation in bioheat transfer: a comparison of particle filter algorithms," *Int. J. Numer. Methods Heat Fluid Flow*, vol. 27, no. 3, pp. 615–638, 2016.
- [42] P. Benner, V. Mehrmann, V. Sima, S. Van Huffel, and A. Varga, "SLICOT-A subroutine library in systems and control theory," in *Applied and Computational Control, Signals, and Circuits SE - 10*, B. Datta, Ed. Boston: Birkhäuser, 1999, pp. 499–539.
- [43] Z.-S. Deng and J. Liu, "Monte Carlo method to solve multidimensional bioheat transfer problem," *Numer. Heat Transf. Part B Fundam.*, vol. 42, no. 6, pp. 543–567, 2002. DOI: [10.1080/10407790260444813](https://doi.org/10.1080/10407790260444813).
- [44] Z.-S. Deng and J. Liu, "Mathematical modeling of temperature mapping over skin surface and its implementation in thermal disease diagnostics," *Comput. Biol. Med.*, vol. 34, no. 6, pp. 495–521, 2004. DOI: [10.1016/S0010-4825\(03\)00086-6](https://doi.org/10.1016/S0010-4825(03)00086-6).
- [45] Y.-G. Lv, Z.-S. Deng, and J. Liu, "3-D numerical study on the induced heating effects of embedded micro/nanoparticles on human body subject to external medical electromagnetic field," *IEEE Trans. Nanobiosci.*, vol. 4, no. 4, pp. 284–294, 2005. DOI: [10.1109/TNB.2005.859549](https://doi.org/10.1109/TNB.2005.859549).
- [46] E. Majchrzak and M. Paruch, "Numerical modelling of the cancer destruction during hyperthermia treatment," presented at the 19th International Conference on Computer Methods in Mechanics CMM-2011, Warsaw, Poland, Short Papers, 2001, pp. 333–334.
- [47] P. A. Hasgall, "ITIS database for thermal and electromagnetic parameters of biological tissues, [online]" 2015. Available from: <https://itis.swiss/virtual-population/tissue-properties/database>. [Accessed January 15, 2018].